BNL-213767-2020-JAAM

Enhancing the partial oxidation of gasoline with Mo-doped Ni catalysts for SOFC applications: An integrated experimental and DFT study

Q. Bkour, J. A. Boscoboinik

To be published in "Applied Catalysis B: Environmental"

June 2020

Center for Functional Nanomaterials

Brookhaven National Laboratory

U.S. Department of Energy

USDOE Office of Science (SC), Basic Energy Sciences (BES) (SC-22)

DISCLAIMER

Enhancing the partial oxidation of gasoline with Mo-doped Ni catalysts for SOFC applications: An integrated experimental and DFT study

Qusay Bkour[a,‡], Fanglin Che[b,‡], Kyung-Min Lee[c], Chen Zhou[d], Nusnin Akter[c,d], Jorge Anibal Boscoboinik[d], Kai Zhao[e], Jake Gray[a], Steven R. Saunders[a,f], M. Grant Norton[a,g], J.-S. McEwen[a,f,h,i,j], Taejin Kim[c]*, Su Ha[a*]

[a]Voiland School of Chemical Engineering and Bioengineering, Washington State University, Pullman, WA 99164-2710, USA

[b]Department of Chemical Engineering, University of Massachusetts Lowell, Lowell, MA, 01854, USA

[c]Department of Materials Science and Chemical Engineering, Stony Brook University, Stony Brook, NY 11794, USA

[d]Center for Functional Nanomaterials, Brookhaven National Laboratory, Upton, NY 11973, USA

[e]School of Materials Science and Energy Engineering, Foshan University, Foshan 528000, China

[f]Department of Chemistry, Washington State University, Pullman, Washington 99164, United States

[g]School of Mechanical and Materials Engineering, Washington State University, P.O. Box 642920, Pullman, WA 99164-2920, USA

[h]Institute for Integrated Catalysis, Pacific Northwest National Laboratory, Richland, Washington 99352, United States

[i]Department of Physics and Astronomy, Washington State University, Pullman, Washington 99164, United States

[j]Department of Biological Systems Engineering, Washington State University, Pullman, Washington 99164, United States

ABSTRACT

We introduce a small amount of Mo atoms into Ni/YSZ catalyst for the partial oxidation reaction of gasoline. Ni-Mo/YSZ catalyst displays a high reforming activity and stability with an isooctane conversion of 90% and H_2 yield of 76% with less degree of coking and sintering compared to Ni/YSZ catalyst. Our XRD results indicate that a Ni-Mo solid solution is formed. Raman results also suggest that a presence of well dispersed Mo=O species over Ni surface can be a possible active site that is related to the high coke resistance of Ni-Mo/YSZ catalyst. DFT-based calculations indicate that Ni-Mo/YSZ catalysts enhance the carbon-tolerance by increasing activation barriers for the C-H bond cleavage and C-C coupling as compared with the Ni/YSZ system. Ni-Mo catalyst is used as an internal micro-reforming layer on top of conventional Ni-YSZ anode supported single cells. The single cell displays a significantly improved stability with a low degradation rate.

KEYWORDS

Carbon tolerance, gasoline partial oxidation, SOFCs, Ni-Mo, and DFT-based calculation.

1. INTRODUCTION

Conventional gas turbine and internal combustion engines generate electricity via fuel combustions, followed by converting the generated heat energy into mechanical energy and finally into electricity. These multiple conversion steps lead to a low overall energy conversion efficiency with large energy loses [1,2]. Solid oxide fuel cells (SOFCs) can convert the chemical energy of liquid transportation fuels and next-generation liquid bio-fuels to electrical energy with a higher efficiency via electrochemical reactions, while they produce less emissions and require less maintenance costs [3,4]. Current methods for operating fuel cells using logistic liquid fuels involve external fuel reforming processors, which add complexity to the overall fuel cell system and increase the device footprint [5]. An internal reforming SOFC technology can combine both SOFCs and external reforming units as one system, and it can offer a much more compact and simple fuel cell system by directly feeding liquid fuels to the anode [6–9]. Among various internal reforming SOFC configurations, introducing a micro-reforming layer over the conventional anode is the most promising path [4]. In this configuration, the fuels are first internally reformed over the micro-reforming layer to generate the synthesis gas followed by its electrochemical oxidation over the anode. Thus, the successful development of internal reforming SOFCs depends on the development of cost-effective and high-performance catalysts with high coking resistance and sulfur tolerance for fabricating its micro-reforming layer. Although several transition metals including Rh, Pt, and Ru are active for liquid fuel reforming [10–13], the cost and availability of noble metals limits their application as the internal reforming catalyst. Ni-based catalysts are a promising alternative to noble metals because they show good activity at a much lower price point [14]. However, coke formation and particle sintering often lead to the rapid deactivation of Ni-based catalysts [15–17]. Controlling the size of a Ni particle is one of the strategies that have been shown to minimize the formation of surface carbon [18]. Carbon nucleation and subsequent growth on the Ni

surface can be limited by preparing small Ni particles in order to improve the catalytic stability during the hydrocarbon reforming [19]. It is generally acknowledged that Ni nanoparticles less than 7 nm in diameter can suppress coking and sintering [20–22]. Another strategy is to use supports with enhanced oxygen storage capacity (OSC) to facilitate the removal of coke and enhance the dispersion of Ni [23]. A solid solution of ceria-zirconia (CZ) is known to have both a high OSC and redox capability, which results in a high coking resistance during reforming reactions [24–26]. More recently, a number of authors have attempted to improve the long-term stability of Ni catalysts by the addition of secondary metals to Ni [4,27–30]. For example, Ni-Sn bimetallic catalysts demonstrate an enhanced carbon tolerance than monometallic Ni during the steam reforming of isooctane [31]. DFT-based calculations indicate that Ni-Sn catalysts have a high propensity to oxidize carbon and that they also lower the driving force to form carbon deposits on low-coordinated metal sites as compared to monometallic Ni [32,33]. Some groups reported that adding Mo-based promoters to Ni catalysts enhances their stability [34,35]. For example, Claudia et al. [36] found that Mo species increases the coking resistance of Ni-Mo/Al_2O_3 catalysts during the dry reforming of methane. According to this previous study, Mo can block the active sites on the Ni metal surface or could be placed on the Ni crystal surface resulting in a dilution effect. Both effects would help to diminish the deposition of carbon. The carbon resistance of Ni-Mo based catalysts during the dry reforming of methane was also explained in terms of the electronic modifications produced by Mo. It was postulated that the addition of Mo (an electron acceptor) leads to a decrease in the adsorption strength of coke on the Ni surface and hence decreases the coking rate [37].

This work aims to improve the activity and stability of supported Ni catalysts by the addition of Mo promoter for partial oxidation (POX) of isooctane and gasoline at high weight-hourly-space-velocity (WHSV) that is consistent with the operating condition of SOFCs. Herein, Ni-Mo

catalysts are used as an internal micro-reforming layer on top of conventional Ni/YSZ anode supported single cells. In this reforming layer/electrochemical anode bilayer design, liquid hydrocarbon fuels are reformed into syngas within the catalytic reforming layer. The resulting gases are then delivered to the anode for the subsequent electrochemical reactions [38,39]. Effects of the micro-reforming layer on the electrochemical performance of the single cells are comparatively investigated by running the cell with an isooctane (or gasoline)/air mixture as fuel. This work also aims to understand how the addition of Mo improves the overall reforming performance of Ni/YSZ catalyst system toward the isooctane (or gasoline) by using a combination of experimental work and *ab initio* quantum mechanics computations.

2. METHODS

2.1 Experimental Section

2.1.1. Catalyst Preparation

Commercial yttrium-stabilized zirconia (YSZ, 8 mole % Y_2O_3, Inframat Advanced Materials) was used to prepare the Ni (11 wt.%)-Mo (3 wt.%)/YSZ sample (with Mo/Ni molar ratio of 1/6) by the wet co-impregnation method. An aqueous solution of ($Ni(NO_3)_2 \cdot 6H_2O$, Alfa Aesar) and ($(NH_4)_6Mo_7O_{24} \cdot 4H_2O$, Alfa Aesar) was mixed with the YSZ support. The sample was then dried overnight at 100 °C, calcined at 500 °C for 4 h (dry pure air, A-L Compressed Gases) and then reduced at 750 °C for 1.5 h in a stream of 50% H_2/He (OXARC). Ni (11 wt.%)/YSZ was synthesized by the same method using an aqueous solution of $Ni(NO_3)_2 \cdot 6H_2O$ without the Mo precursor. Ni (11 wt.%)-Sn (3 wt.%)/YSZ was also synthesized by the same method using aqueous solutions of $Ni(NO_3)_2 \cdot 6H_2O$ and $SnCl_2 \cdot 2H_2O$ (Sigma-Aldrich). Both Ni (11 wt.%)/YSZ and Ni (11 wt.%)-Sn (3 wt.%)/YSZ samples were used as reference catalyst materials for the comparison.

2.1.2. Single Cell Fabrication

The anode supported coin-type single cells with a configuration of porous Ni-YSZ anode support/YSZ/$Ce_{0.8}Sm_{0.2}O_{1.9}$ (SDC) bi-layer electrolyte/$La_{0.6}Sr_{0.4}Co_{0.2}Fe_{0.8}O_{3-\delta}$ (LSCF) cathode were fabricated by a dry-pressing and spin-coating process. The detailed fabrication procedure was reported in our previous paper [40].

The micro internal reforming layer was fabricated by painting the Ni-Mo/YSZ catalyst on a Ni metal mesh. The catalyst paste was prepared by mixing 20 wt.% Ni-Mo/YSZ powder with a slurry containing 2.4 wt.% binder (Butvar B-98, Sigma-Aldrich) and 77.6 wt.% ethanol. A total of ~20 mg of Ni-Mo/YSZ catalyst was painted on both sides of the Ni mesh to form the micro internal reforming layer. This internal reforming layer was attached to the anode of the single cell for electrochemical performance evaluation [41].

2.1.3. Catalyst Characterization

The crystalline phases in the fresh and spent catalysts were determined by powder X-ray diffraction (XRD) using a Rigaku Miniflex 600 diffractometer with Cu Kα radiation operated at 40 kV voltage and 15 mA current. The XRD patterns were collected at a scanning step size of 0.01° with a scanning rate of 1 °/min in a 2θ range from 20° to 60°. Transmission electron microscopy (TEM) was used to investigate the morphologies of the catalysts using a FEI Technai G2 20 Twin at 200 kV. Temperature-programmed reduction (TPR) measurements were performed in a chemisorption system (ChemiSorb 2720, Micromeritics). The following procedure was used for TPR: 100 mg of sample was placed in a quartz U-tube and pretreated with flowing pure He (A-L Compressed Gases) at 50 mL/min at room temperature. Following the pretreatment, 10% H_2/He (OXARC) was introduced at the same flow rate for temperatures ranging from 25–900 °C with a heating rate of 10 °C/min. The amount of carbon deposited on the surface of the spent catalysts

was quantified using thermogravimetric analysis (TGA) under dry pure air (A-L Compressed Gases) using TA Instruments Q50. Samples were loaded in platinum crucibles and then heated with air from room temperature to 800 °C at a rate of 5 °C/min. Molecular structure and bonding vibration of the fresh and spent Ni-Mo/YSZ samples were determined via Raman spectroscopy at room temperature with a Renishaw-inVia Raman microscope equipped with a confocal microscope and 3600 grooves/mm gratings. For comparison, bulk YSZ, Mo/YSZ, and Ni/YSZ Raman spectra were also collected. The laser excitation at 325 nm was generated from the He-Cd laser (Kimmon, Model: IK3201R-F). The scattered photons were directed into a single monochromator and focused onto an air-cooled charge-coupled device. The Raman shift was calibrated with a Teflon (731 cm^{-1}). The spectral acquisition times were 20 scans accumulated with 50 sec/scan. The Raman spectra of the carbon phase on the spent samples were collected by the visible Raman spectrometer (BaySpecNomadic^{TM} Raman Microscope) equipped with a confocal microscope (Olympus BX-51 upright microscope), Volume Phase Gratings (VPG), and a dichroic filter. The spent samples were excited with 532 nm excitation (DPSS CW, diode-pumped solid state continuous wave, single-mode, open beam, max power output 50 mW) in the 1200-1800 cm^{-1} Raman shift regions. The visible 532nm Raman spectra were collected through a CCD detector (2048 x 64 pixels). The spectral acquisition times were 10 scans accumulated with 30 sec/scan. X-Ray photo-electron spectroscopy (XPS) was performed on a SPECS Phoibos 100 hemispherical analyzer to characterize the composition and surface chemistry. Typically, Al Kα (1486.6 eV) was used as the X-Ray source. The surface charging effect was compensated through a calibration by applying the binding energy (BE) of C1s (BE=284.6 eV) as an internal standard. Powder samples were mounted on a copper plate by pressing two copper plates against each other under 5 MPa. Then the copper plate was attached to the sample holder by copper tape.

2.1.4. Electrochemical Performance of Fuel Cell

Electrochemical performances of the anode-supported single cells with the Ni-Mo/YSZ catalytic reforming layer were evaluated using a lab-designed fuel cell testing system. The system consisted of an Autolab electrochemical workstation (Metrohm Autolab M101), a DC electric load (BK precision 8500), a set of mass flow controllers (Brooks 8580E), and alumina sample holders. An alumina-based ceramic binder (AREMCO Products) was used as the gas sealing material. The single cell was heated to 750 °C and the anode was reduced in hydrogen. The performance of the single cell was first tested using H_2 (50 ml/min) as fuel. The fuel was then changed to a mixture of isooctane and air by flowing air through an isooctane bubbling system at a flow rate of 90 ml/min at 25 °C. Electrochemical impedance spectra of the single cell were obtained under open-circuit voltage (OCV) conditions in the frequency range of 0.01 Hz to 100 kHz. The amplitude of the input sinusoidal signal was set to be 10 mV [41].

2.1.5. Isooctane Catalytic Reforming Tests

The partial oxidation reaction was carried out in a fixed-bed quartz reactor (300 mm length, 7 mm internal diameter). In a typical experiment, 100 mg of the reduced catalyst was loaded into the quartz reactor and held in place by a quartz wool plug. The temperature of the catalyst bed was maintained at 750 °C for all reforming tests. A K-type thermocouple (Omega) was placed at the center of the catalyst bed to record and control its temperature. The inlet and outlet temperatures of the catalyst bed were measured during the reforming reaction of isooctane at 750 °C and no temperature changes were observed. A silicon carbide bed was placed 5 cm upstream from the catalyst bed to enhance the mixing of the reactants. The reactant feed was composed of isooctane and air at an O_2/C ratio of 0.5 using a flow rate of 2 mL/h (liquid) and 90 ml/min (gas), respectively (WHSV of 13.8 h^{-1}) at atmospheric pressure. A calibrated mass flow controller and syringe pump were used to control the flow rates of air and isooctane, respectively. The exit stream was cooled

down to 5 °C before it was sent to a gas chromatograph. The dry gaseous products were then analyzed using the gas chromatograph equipped with two packed columns (Molecular Sieve 13X and HayeSep D) and a TCD detector.

2.2 Computational Setup

The DFT calculations were carried out with the Vienna *Ab Initio* Simulation Package (VASP) code [42,43]. The exchange-correlation interactions were treated using the Perdew-Burke-Ernzerhof (PBE) [44] functional and the projector-augmented wave (PAW) method was applied [45] to solve the ion-electron interactions in the periodic system. The pseudopotential version (PAW_PBE) for each element is listed here: 07Sep2000 for Zr_sv, 08Apr2002 for O, 06Sep2000 for Y_sv, 06Sep2000 for Ni, and 08Apr2002 for Mo [46]. The size of the Ni/YSZ (or Ni-Mo/YSZ) slab was 7.25 Å × 12.56 Å [47–50]. We used a Monkhorst-Pack mesh [51] with a (4 × 2 × 1) kpoint grid and a plane wave expansion up to 400 eV. This computational setup ensured that the oxygen vacancy formation energy inside the Ni/YSZ slab differs by less than 0.03 eV as compared to a more-dense (4 × 4 × 1) kpoint grid and a higher energy cutoff of 500 eV. The Ni/YSZ (or Ni-Mo/YSZ) cermet included a three-layer YSZ slab and an 18-atom Ni cluster (or an 18-atom Ni cluster with one Mo atom dopant) and a 12 Å vacuum layer separation between each periodic unit cell as shown in Fig. SI 8. When we performed a Bader charge analysis, we applied a fast Fourier transform (FFT) grid that was twice as dense as compared to the standard FFT grid so as to ensure that the Bader charge results were fully converged. More details about the computational setup were given in our previous works [52–56].

3. RESULTS AND DISCUSSION

3.1 Catalyst Characterization

To obtain insight into the reduction process of the calcined samples, an H_2-TPR experiment was performed. The H_2-TPR profiles of YSZ supported Ni and Ni-Mo catalysts calcined at 500 °C are shown in Fig. 1. For Ni/YSZ, the single peak located at around 350 °C is attributed to the reduction of NiO to metallic Ni [57]. The Ni-Mo/YSZ reduction peak is shifted to higher temperatures at around 450 °C, which could be related to the improvement of the metal-support interaction and enhancement of the Ni dispersion over YSZ supports (Table SI. 1) after the addition of Mo species [58]. The catalysts following the H_2 reduction were characterized by a XRD analysis prior to the reaction to determine their crystalline phases and average crystallite sizes. The XRD patterns of Ni/YSZ and Ni-Mo/YSZ catalysts after reduction treatment at 750 °C are shown in Fig. 2. Both samples clearly showed diffraction peaks corresponding to YSZ [59,60]. Specifically, XRD patterns for the YSZ supported metal catalysts contain higher intense peaks at ~28.3° and ~31.5° for the m-ZrO_2 phase as compared to the pristine YSZ (t-ZrO_2 dominant, ~30°, not shown for brevity). As such, the surface species (Ni or Ni-Mo) can cause the metastable t-ZrO_2 transformation into a stable m-ZrO_2. The m-ZrO_2/t-ZrO_2 peak ratio in the Ni-Mo/YSZ XRD pattern is higher than that of Ni/YSZ, which indicates that the presence of Mo can improve the stability of YSZ. The nickel oxide (NiO) phase was entirely transformed into metallic nickel (Ni) after the reduction step, as deduced from the absence of peaks associated to the NiO phase (2Θ = 37° and 43°) and the appearance of the metallic Ni (2Θ = 44° and 52°). With the addition of Mo, the main diffraction peak of the Ni metal (2Θ = 44.5°) is shifted to a lower 2Θ value. This is attributed to the expansion of the Ni lattice due to the partial substitution of a Ni atom ($r \approx 1.35$ Å) by a larger Mo atom ($r \approx 1.45$ Å) during the formation of a Ni-Mo solid solution. Moreover, with the addition of Mo, the metallic Ni peak broadens and decreases in intensity, suggesting that the Ni particles are well dispersed on the YSZ support. The Scherrer equation was used to calculate

the average crystallite size of the metallic Ni phase, as reported in Table SI 1. The average crystallite size for Ni-Mo/YSZ is 8.2 nm while Ni/YSZ is 16.1 nm, which indicates that a higher degree of sintering took place for the sample without Mo during thermal treatment. It can be hypothesized that increased YSZ stability with the addition of Mo can possibly reduce the agglomeration of Ni particles.

3.2 Effect of Mo on the Catalytic Performance

Isooctane partial oxidation (POX) was carried out over Ni/YSZ and Ni-Mo/YSZ catalysts under O_2/C of 0.5, 750 °C, atmospheric pressure, and WHSV of 13.8 h^{-1}. As shown in Fig. 3, the Ni-Mo/YSZ catalyst is stable over 24 h of time-on-stream (TOS) with a conversion of 97%, H_2 yield of 73%, and CO yield of 80%. The molar ratio between H_2 and CO is about 0.92 (which is lower than the stoichiometric ratio). This difference indicates the possible occurrence of the reverse-water gas shift (RWGS) reaction that consumes some of the H_2 products during the partial oxidation process [26]. Beside the RWGS reaction, there could be other side reactions including the complete oxidation and methanation which can affect the final carbon conversion and product yields[18,61]. The Ni/YSZ sample shows a severe deactivation after only 8 h of TOS. Consequently, its conversion decreases to 45% while both H_2 and CO yields drop to 21% at a TOS of 24 h. In this work, the partial oxidation reaction was operated at a relatively high space velocity (WHSV of 13.8 h^{-1}) of the fuel stream containing 5 mol% of isooctane in order to produce enough syngas to operate the fuel cell. There are few other publications which used different catalysts for the partial oxidation of isooctane/gasoline (Table SI. 2). However, they either operated at a lower fuel content (i.e., a lower amount of isooctane/gasoline catalytically processed per unit time) than one we used in this study or showed lower stability as compared to the Ni-Mo/YSZ catalyst. For example, Pengpanich et al. prepared a Ni(5 wt.%)Sn(0.5 wt.%)/$Ce_{0.75}Zr_{0.25}O_2$ catalyst for the POX

of isooctane at a O_2/C ratio of 0.5, 1 mol% of isooctane in the feed stream, and 700 °C [62] After a time-on-stream of 12 h, the isooctane conversion was only 73 %, while the total carbon deposition was 2.2 wt.%. When the Sn loading is changed from 0.5 wt.% to 2 wt.% the conversion after 12 h time-on-stream dropped to 51 % [62]. As compared to our current study, Pengpanich et al [62]. operated their Ni-Sn bimetallic catalysts at more diluted isooctane in the feed stream (1 mol% vs. 5 mol%). Despite these less severe operating conditions, our Ni-Mo bimetallic catalyst in this present study still outperformed previously studied Ni-Sn bimetallic catalysts. MoO_2 was also tested for the POX of premium gasoline (with 37% aromatics) and compared its performance with a Ni catalyst at O_2/C = 0.72, 1.6 mol% of isooctane in the feed stream, WHSV = 0.6 h^{-1}, and T = 700 °C [63]. Based on its reforming data, MoO_2 catalysts were active and stable after 7 h time-on-stream with a carbon conversion and a H_2 yield of 100 and 94%, respectively, while Ni catalysts showed severe deactivation due to the formation of carbon [63]. MoO_2 is a very promising catalyst for the POX of various logistic fuels. However, its phase stability is very low: it can easily oxidize into MoO_3 phase if O_2/C ratio is too high (e.g. O_2/C is higher than 0.7) while it can easily reduce into metallic Mo or a Mo_2C phase if the O_2/C ratio is too low (e.g. if the O_2/C ratio is lower than 0.6) [63]. Its stability window is very small such that it has many challenges for implementing it to the practical applications where O_2/C ratio would fluctuate a lot. Unlike MoO_2, our Ni-Mo/YSZ in the present study uses Mo as the promoter and it does not possess any bulk MoO_x phases. Thus, its phase stability was not affected even at the stoichiometric O_2/C ratio for POX of isooctane.

XRD was used to estimate the average crystallite size of the spent sample and verify the formation of carbon deposition. Fig. 4 shows that there is a diffraction peak at 26.6° for the Ni/YSZ sample, which is attributed to the formation of carbon deposits. Moreover, the spent Ni/YSZ sample shows a significant increase in its average crystallite size from 16.1 to 26.1 nm (Table SI.

1). The Ni-Mo/YSZ spent sample, however, shows no indication of carbon formation (Fig. 4 (B)) and much less nanoparticle aggregation (from 8.2 nm to 10.3 nm) during the isooctane reforming reaction. It should be noted that the presence of small size or amorphous carbon species, which could not be detected by using the XRD, cannot be ignored. The formation of different carbon phases on Ni/YSZ and Ni-Mo/YSZ will be explained in more detail in the corresponding Raman spectroscopy measurements. The combination of sintering and coking resistant natures of Ni-Mo/YSZ catalyst allows the reaction to run stably for 24 h. These results are confirmed by TEM images of fresh and spent catalysts as shown in Fig. 5. It is clearly observed that whisker carbon is formed on the spent Ni/YSZ sample, while no such carbon is observed on the spent Ni-Mo/YSZ sample. It can be concluded that the addition of Mo to a Ni/YSZ catalyst can effectively reduce the growth of carbon whiskers. Huang et al. [64] reported that Mo species play an important role in reducing the amount of shell-like carbon deposits which encapsulate the Ni particles. It was also reported that strong metal-support interactions lead to a higher dispersion of Ni nanoparticles, prevents Ni-Mo metal particles from being physically lifted up off of the support during the carbon growth process, and limits the encapsulation of the Ni particles by carbon [65]. Our results agree with other reports [66,67] that adding different promoters to prevent Ni agglomerations and to increase the interaction between Ni nanoparticles and the support, whose combined effects can mitigate the formation of carbon.

To measure the resilience of the Ni-Mo/YSZ catalyst against coking, we tested it using premium gasoline (octane rating of 91~94) as fuel with an aromatic content of approximately 35 vol% [68]. Based on its CHO elemental analysis, its composition is approximated as $C_{7.14}H_{14.3}$. Aromatic compounds are considered coking precursors and therefore, a high rate of coke formation can be expected when using aromatic-rich fuels. The operation conditions for the test are the same

as isooctane reforming conditions (O_2/C=0.5, WHSV=13.8 h^{-1}, and T=750 °C). As shown in Fig. 6, even after 12 h of TOS, the catalytic performance exhibited by Ni-Mo/YSZ is fairly stable with a H_2 yield of 76% and a conversion of 90%. However, the Ni/YSZ sample starts with relatively poor initial performances, worsening after around 6 h of TOS. The low performance observed with the Ni/YSZ catalyst is the direct result of coke formation, which eventually clogged the reactor and significantly reduced its catalytic performance. XRD analysis of the spent samples (Fig. SI 1) shows a much more intense peak for carbon deposition on the Ni/YSZ sample as compared to that of the Ni-Mo/YSZ sample. Furthermore, the spent Ni/YSZ sample shows an increase in its average crystallite size from 16.1 to 26.8 nm (Table SI 3), which is a similar result that is observed for the isooctane reacted sample (Table SI 1).

To investigate the oxidation state of our catalyst samples, we have performed XPS measurements. The Ni $2p_{3/2}$ XPS spectra of fresh Ni-Mo/YSZ and Ni/YSZ catalysts are shown in Fig. SI 2 (A). For the fresh Ni/YSZ sample, there is a strong peak at a core level binding energy (CLBE) of ~855.8 eV, which can be assigned to the metallic Ni (Ni^0). This metallic Ni peak up-shifts by ~0.3 eV for the fresh Ni-Mo/YSZ sample, which suggests that Ni is partially oxidized by the presence of Mo. For the spent Ni-Mo/YSZ sample, although the peak intensities around a CLBE of ~856.1 eV are very week, it clearly shows that the peaks still remain in the spent Ni-Mo/YSZ spectrum (Fig. SI 2 (B)). In the case of Ni/YSZ sample, however, the Ni metal peak at a CLBE ~855.8 eV disappeared after the isooctane and the gasoline POX reaction (Fig. SI 2 (C)), which indicates that Ni particles were fully covered by the thick carbon deposition.

A TGA analysis is used to obtain quantitative information regarding the deposition of carbon on the catalyst surface after the partial oxidation of gasoline. As shown in Fig. 7, weight loss due to the carbon oxidation is started at ~500 °C [69,70]. The Ni/YSZ sample shows a much higher weight

loss (~80 wt.%) at 700 °C, which may be attributed to the presence of the larger amount of coke that is formed as compared to that of the Ni-Mo/YSZ sample (~17 wt.%). The derivative peak of the TGA curve (Fig. SI 3) for the spent Ni/YSZ catalyst is shifted to a higher temperature (~660 °C) as compared to that of the spent Ni-Mo/YSZ catalyst due to a higher degree of graphitization of the coke deposit [71].

Tin (Sn) is another promoter that has been widely used to improve the stability of catalysts during liquid fuel reforming by reducing the Ni ensemble size and preventing surface coking. The Linic group found that Ni-Sn bimetallic systems have a lower thermodynamic driving force for the formation of coke, which is associated with the nucleation of carbon atoms on low-coordinated Ni sites [32]. Ni-Sn demonstrated an enhanced reforming performance as compared to that of monometallic Ni in the steam reforming of isooctane, methane, and propane [32,33]. Pengpanich et al. [62] tested Ni-Sn systems for the POX of isooctane (O_2/C ratio of 1 and gas-hourly-space-velocity (GHSV) of 80,000 h^{-1}) at 700 °C and found a conversion of 73% with only 2.2 wt.% carbon deposits after 12 h of TOS. For the present study, the catalytic performance of Ni-Mo/YSZ for the POX of isooctane is compared to that of Ni-Sn/YSZ under the same reaction conditions (WHSV of 13.8 h^{-1}, GHSV of around 100,000 h^{-1}, and O_2/C ratio of 0.5). It is worthwhile to note that the reforming conditions used by this present study for Ni-Mo/YSZ system are harsher than those of Pengpanich et al's. Use of NiSn/YSZ catalysts results in poor isooctane conversion and H_2 selectivity: a conversion of 67% and H_2 yield of 18% after 24 h of TOS (Fig. SI 4). This performance is not much higher than that of the non-catalyzed gas-phase reaction (45% conversion and 15% H_2 yield), indicating that Sn is not suitable to mitigate carbon formation and enhance the activity of Ni-based catalysts at these harsh operating conditions. The XRD analysis of the spent

NiSn/YSZ catalyst indicates that carbon deposits are formed after operating the reactor for 24 h (Fig. SI 5).

Over the past several decades, Raman spectroscopy has elucidated fundamental information about the nature of the catalytically active sites for the supported metal and the metal oxide in a heterogeneous catalyst, where metals or metal oxides are present as a two-dimensional surface layer (67–70). In order to understand the molecular structure of a fresh, isooctane-reacted, gasoline-reacted YSZ supported catalysts as well as the carbon species on the spent catalysts, we characterized these samples by UV- and visible-Raman spectroscopy. The UV-Raman spectra of a fresh YSZ, Ni/YSZ, Mo/YSZ, and Ni-Mo/YSZ samples are shown in Fig. 8 (A). The Raman spectrum of the YSZ sample contains several bands at 320 (medium), 378 (weak), 470 (medium), and 630 (strong) cm^{-1}, which are characteristic of a tetragonal-ZrO_2 (t-ZrO_2) and a monoclinic-ZrO_2 (m-ZrO_2) phase [72,73]. The intensity ratio of the 470 and the 630 cm^{-1} bands (I_{630}/I_{470}) has been applied to distinguish the ZrO_2 phase [74]. The higher intensity of the 630 cm^{-1} band as compared to the 470 cm^{-1} band ($I_{630} > I_{470}$) indicates that the YSZ sample possesses a dominant t-ZrO_2 phase. In the case of the YSZ supported catalysts, the intensity of the Raman band at 630 cm^{-1} decreases dramatically as compared to the YSZ sample and a new weak band appears at 613 cm^{-1}, which is characteristic of m-ZrO_2 [73]. These results suggest that the presence of surface metals, such as Ni and Mo, and a reduction temperature transform the zirconia phase partially from a t-ZrO_2 to a m-ZrO_2 during the synthesis of a YSZ-supported mono- or bimetallic catalyst, which is consistent with the XRD results. The Raman spectrum of the Mo/YSZ catalyst gives rise to new Raman bands at 850 (strong) and 962 (weak) cm^{-1} that can be assigned to the asymmetric and the symmetric stretching mode of the Mo=O terminal bond [75–77], respectively. It has been reported that at a higher MoO_x loading, for instance, a monolayer or oligomerized MoO_x species, the stretching M=O band

is shifted from < ~980 cm^{-1} to > ~1000 cm^{-1} in addition to the dioxo (O=Mo=O) transformation to mono-oxo (Mo=O) [78]. Due to the low Mo wt% used to prepare our Mo/YSZ catalyst sample and a lack of its Raman band at > ~1000 cm^{-1} (Fig. 8 (A)), we can possibly avoid the presence of a monolayer or oligomerized MoO_x species for the Mo/YSZ sample. Instead, we hypothesize that the MoO_x surface species are well-dispersed without agglomeration on the YSZ support. The Raman spectrum of Ni/YSZ exhibits a weak peak intensity at ~800 cm^{-1} in addition to the mixed bands that are characteristic of the t-ZrO_2 and the m-ZrO_2 phase. The assignment of the band at ~800 cm^{-1} is not clear, but it can be the part of the YSZ sample after t-ZrO_2 partially transforms to m-ZrO_2. The Raman spectrum of Ni-Mo/YSZ is very similar to that of Ni/YSZ, except for the band at 906 cm^{-1}, which is assigned to the asymmetric stretching mode of the well-dispersed Mo=O terminal bond [76,79,80]. Based on our XPS data, the surface Ni is partially oxidized for the Ni-Mo/YSZ sample. However, the NiO_x Raman band, which typically shows up between 500 cm^{-1} and 600 cm^{-1} [81], is absent in our Ni/YSZ and Ni-Mo/YSZ samples. Thus, it seems that only the surface electronic structure of Ni is affected by the presence of Mo, while the Ni subsurface clusters are fully reduced.

To further understand the nature of the coke (or carbonaceous) species after the interaction with isooctane and gasoline, the spent catalysts were investigated by visible-Raman spectroscopy. As shown in Fig. 8 (B) and (C), two intense peaks dominate at ~1340 cm^{-1} and ~1570 cm^{-1}, which are attributed to the disordered sp^2 carbon networks or the presence of structural defects in the graphitic structure (D-band) and the stretching vibration of the ordered sp^2 C-C or graphitic phase (G-band), respectively [82,83]. The Raman spectra of the isooctane (Fig. 8 (B)) and gasoline (Fig. 8 (C)) reacted catalysts show the higher D band intensity than that of the G band, which indicates that the spent catalysts have a relatively more disordered graphitic carbon. It should be noted that

the intensity ratios (I_G/I_D) between G and D bands for the isooctane and the gasoline reacted Ni/YSZ and Ni-Mo/YSZ sample catalysts clearly show that Ni/YSZ sample contains more graphitic carbon as compared to that of the Ni-Mo/YSZ sample. Although the Raman spectroscopy can't provide quantitative information of carbon deposition, we can get a better idea when we combine these results with our XRD and our TGA analysis. As such, we expect that higher total amounts of graphitic carbon species were formed for the spent Ni/YSZ sample under the harsh reforming reaction conditions. There is one substantial difference between the isooctane and gasoline reacted Ni-Mo/YSZ Raman spectra. Indeed, we notice that the Mo=O band at 906 cm^{-1} disappears after the gasoline reforming reaction (Fig. SI 6), while the Mo=O band in the isooctane reacted Ni-Mo/YSZ spectrum remains. To confirm the regeneration of Mo=O band, the gasoline reacted sample was treated under oxidizing and reducing conditions. As shown in Fig. 8 (D), the regenerated Ni-Mo/YSZ spectrum is very similar to the fresh sample's spectrum including the M=O band at 906 cm^{-1}. This result suggests that the Mo=O bond was only physically covered by carbon species without changing of MoO_x molecular structure. MoO_x-based catalysts have shown reforming activity for liquid hydrocarbons (including isooctane) with high coking resistance [63,84]. The catalytic activity of the MoO_x sample can be explained by the dual metallic-acidic character of these species as well as its remarkable oxygen mobility [63,85]. The high oxygen mobility enhances catalytic activity, which can be explained in terms of a Mars-van Krevelen mechanism. According to this mechanism, the hydrocarbon molecules are first adsorbed on the metal oxide surface. The next stage in the mechanism involves the oxidation of adsorbed hydrocarbons following the insertion of oxygen atoms provided by the reduction of the metal oxide surface. The reduced metal oxide surface is re-oxidized and surface oxygen vacancies are replenished by gas-phase oxygen [84,86].

In summary, TEM, XRD and TGA results confirm that a Ni-Mo/YSZ catalyst has less carbon deposits as compared to the spent Ni/YSZ catalyst, and our Raman spectroscopy analysis demonstrates that the relative amount of graphitic carbon species on the spent Ni/YSZ sample was higher than that of Ni-Mo/YSZ sample (which was also confirmed by our TGA results). Our XRD measurements suggest that Mo is incorporated into the Ni lattice (by partial substitution of Ni atoms by larger Mo atoms) forming a Ni-Mo solid solution for its bulk phase. Our XPS data suggest that the interaction between surface Ni and Mo atoms for the Ni-Mo/YSZ sample partially oxidizes the surface Ni atoms. Besides the Ni-Mo bimetallic nanoparticles with its solid solution bulk phase and partially oxidized surface Ni, Raman results also suggest that well-dispersed MoO_x species over Ni nanoparticles, especially Mo=O bond, could promote the coke resistance and catalyst stability of Ni-Mo/YSZ catalyst sample.

3.3 Electrochemical Performance of Ni-Mo/YSZ as Internal Reforming Anode SOFC

Ni-Mo/YSZ catalysts were applied as an internal micro-reforming layer over a conventional Ni-YSZ anode. In this reforming layer/electrochemical anode bilayer design, liquid hydrocarbon fuels are reformed to syngas within the catalytic reforming layer. The resulting gases are then delivered to the anode for the subsequent electrochemical reactions (Fig. 9). Fig. SI 7 shows the electrochemical performance of the single cell in H_2 and isooctane/air, respectively. Fig. SI 7 (A) shows current-voltage curves of the single cell at 750 °C. The cell exhibits an open circuit voltage of 1.03 V and a maximum power density of 613 mW cm^{-2} in H_2. The data is comparable with our previously reported results on SOFC single cells with similar configurations [41,87]. When changing the fuel from H_2 to isooctane/air, the open circuit voltage dropped to 1.01 V and the maximum power density decreased to 452 mW cm^{-2}. The decreased performances were mainly caused by the lower concentration of H_2 in the syngas stream generated from the reforming layer (i.e. the syngas

stream did not have 100% H_2) [4]. Fig. SI 7 (B) shows Nyquist plots of the single cell under OCV conditions in H_2 and isooctane/air, respectively. Ohmic and polarization resistances of the single cell were determined by fitting the impedance spectra using Zview software (Table SI 4). By changing the fuel from H_2 to isooctane/air, the ohmic resistance (R_{ohm}) increased slightly from 0.23 to 0.25 Ω cm^2 while the polarization resistance (R_p) increased from 0.37 to 0.50 Ω cm^2. The higher polarization resistance of the single cell in the isooctane/air system was mainly due to the lower H_2 concentration in the syngas stream, which leads to a lower maximum power density as shown in Fig. SI 7 (A). To study the effects of the catalytic reforming layer on the stability of the single cell running on isooctane, the electrochemical performance was measured under a constant current of 500 mA cm^{-2} as shown in Fig. 10. During the 15 h performance stability test, the cell with the reforming layer displays a low degradation rate, while the cell performance without reforming layer stopped in 12 h. Such improved stability demonstrates the great benefits of using a catalytic reforming layer on the electrochemical performance of the single cell under isooctane/air operating conditions.

3.4 DFT studies

For our Ni-Mo bimetallic catalyst system, its bulk phase consists of a Ni-Mo solid solution phase (based on XRD) and its surface also consists of well-dispersed MoO_x species (based on Raman) with the partially oxidized Ni surface (based on XPS). Even though our experimental data cannot clearly pinpoint the presence of the Mo-doped Ni site at the surface, we strongly believe that there is a high probability of having such a site for our Ni-Mo bimetallic catalyst sample because its bulk phase must influence its surface composition. The main purpose of DFT-based calculations in this manuscript was to investigate the surface structure of the Mo-doped Ni site and how it would mitigate the surface coking as compared to a Ni site without a Mo dopant. To

understand the effects of the addition of Mo dopant into Ni lattice on coke prevention in the Ni/YSZ system during the partial oxidation of isooctane, we first determined the most favorable configurations in our model systems (Ni/YSZ and Ni-Mo/YSZ) by calculating their corresponding phase diagrams from first principles (Fig.11). Our Ni-Mo bimetallic catalyst consists of 11 wt.% Ni and Mo 3 wt.% Mo with Mo/Ni molar ratio of 0.16. For our DFT model, we used a Mo/Ni molar ratio of 0.06 since a fraction of the Mo species form well-dispersed MoOx species as discussed in our Raman experimental data. The Gibbs free energy change (ΔG) was obtained as a function of the hydrogen chemical potential ($\Delta\mu_H$), which provides us with a direct connection between our DFT-based model and the relative equilibrium stabilities with different oxygen vacancy concentrations under various experimental conditions [88–91]. Our first principles-based phase diagram (Fig. 11 (A) and (B)) gives us the most stable configurations for the Ni/YSZ and the Ni-Mo/YSZ (2Vbulk) systems, which are those shown Fig. 11 (C) and (D) when the hydrogen partial pressure is between 0.1 and 1 atm. More details regarding the definition of ΔG, the configurations considered, nomenclatures for various Ni/YSZ and Ni-Mo/YSZ models are given in Fig. SI 8 – SI 10, respectively.

We then studied the electronic interactions between the Ni (or Ni-Mo) cluster and the YSZ slab in the most favorable configurations of Ni/YSZ and Ni-Mo/YSZ via a differential charge analysis. As shown in Fig. 12, a larger charge exchange occurs between the Ni-Mo cluster and the YSZ surface as compared to the Ni/YSZ system. A Bader charge analysis also quantitatively validates the integration of the electron cloud in the differential charge density analysis, where the Ni-Mo cluster is more positively charged than the pure Ni cluster, especially near the Mo atom. This indicates the Ni-Mo cluster exists in a more stabilized form with a higher oxidation state as compared to the one in the absence of Mo when adsorbed on the YSZ slab.

To determine how the addition of Mo prevents the formation coke during the partial oxidation of isooctane, we modeled the adsorption of CH (Fig. SI 11), the subsequent cleavage of the C-H bond (Fig. 13) as well as the C-C coupling (Fig. 14) reaction, since they are essential steps in the formation of coke. Based on the DFT-computed adsorption energies, we determined that the most favorable configurations for the adsorption of CH over a Ni/YSZ surface in the presence and in the absence of Mo are similar (Fig. SI 11). To form carbon species, one of the main steps of the partial oxidation of isooctane reaction is the cleavage of the C-H bond. As shown in Fig. 13, we find an activation energy and a corresponding reaction energy of 1.19 eV and 0.89 eV, respectively, for the C-H bond cleavage reaction over a Ni-Mo/YSZ surface, which are significantly higher than those over a Ni/YSZ catalyst (0.98 eV and 0.37 eV). This suggests that the formation of elementary carbon species in the Ni-Mo/YSZ system is harder as compared to the Ni/YSZ system.

We also examined the C-C coupling reaction over Ni/YSZ in the presence and absence of Mo. To accomplish it, we have tested different possible adsorption sites for the coadsorption of C atoms for Ni/YSZ (Fig. SI 12) and Ni-Mo/YSZ (Fig. SI 14). Based on Fig. SI 12 and Fig. SI 14, we only found one configuration for each catalyst system to be stable or to not alter the structure of the Ni-based cluster (Configuration (c) shown in Fig. SI 12 for Ni/YSZ and Configuration (e) shown in Fig. SI 14 for Ni-Mo/YSZ). These two stable configurations were used for our transition state calculation for the C-C coupling pathway shown in Fig. 14. We have also tested various adsorption configurations for the adsorption of the C=C adspecies that are shown in Fig. SI 13 and Fig. SI 15 of the Supporting Information. As shown in Fig. 14, the activation barrier of the C-C coupling over the Ni-Mo/YSZ system is ~0.8 eV higher than that over the Ni/YSZ system. This further suggests that the coke formation is more difficult with the addition of Mo into Ni catalytic system. Similar results can also be found on the Ni (111) flat surface with and without Mo (Fig.

SI 16 and SI 17). In addition, to deconvolute the strain effects coming from the YSZ support in the Ni or the Ni-Mo systems, we examined the projected density of states (PDOS) of the Ni 3*d* orbital in Ni(111) (Fig. SI 18) with and without Mo. The *d*-band center of the Ni atom located in close proximity of the Mo atom shifts away from the Fermi level (Fig. SI 18), suggesting the adsorbed C atom has less electronic interaction with the Ni atom nearby Mo. Consequently, there would be less adsorbed carbon in the Ni-Mo system. This correlates well with our experimental findings that less amount of coke formation on Ni-Mo sample as compared to that of Ni sample.

In summary, we theoretically investigated the C-H bond cleavage and C-C coupling reactions over Ni/YSZ in the presence and absence of Mo dopant into the surface Ni cluster as well as in the presence and absence of YSZ support. These two elementary reactions have higher activation barriers over the Mo-doped Ni catalyst site as compared to the pure Ni catalyst site without the Mo dopant. The theoretical DFT results again correspond well with our experimental results that the Ni-Mo/YSZ catalyst can successfully prevent coking during the partial oxidation of isooctane.

CONCLUSIONS

Carbon-induced catalyst deactivation is one of the main problems associated with the catalytic reforming of liquid hydrocarbons over supported Ni catalysts. Our XRD, TEM, TGA, XPS, and Raman results demonstrate that the Ni-Mo/YSZ catalyst is more carbon-tolerant than Ni/YSZ for the partial oxidation of isooctane and gasoline at high fuel flow rates. Our catalyst studies demonstrate that Ni-Mo/YSZ samples possess an excellent catalytic performance in terms of carbon conversion (97%) and H_2 yield (73%) for the POX of isooctane as compared to that of the unpromoted catalyst. Our XRD measurements suggest that Mo is incorporated into the Ni lattice (by partial substitution of Ni atoms by larger Mo atoms) forming a Ni-Mo solid solution for

its bulk phase. Our XPS data further suggest that the interaction between surface Ni and Mo atoms for the Ni-Mo/YSZ sample partially oxidizes the surface Ni atoms. Besides the Ni-Mo bimetallic nanoparticles with its solid solution bulk phase and partially oxidized surface Ni, Raman results also indicate that well-dispersed MoO_x species over Ni nanoparticles, especially Mo=O bond, could promote the coke resistance and catalyst stability of Ni-Mo/YSZ catalyst sample. Ni-Mo/YSZ catalysts are also applied as the reforming layer over conventional Ni-YSZ anode-based SOFCs. Under isooctane/air operating conditions, an initial maximum power density of 452 mW cm^{-2} is achieved together with high stability and much-improved coking resistance compared to the Ni-based SOFC without the reforming layer. DFT-based calculations were used to investigate the surface structure of the Mo-doped Ni site and how it would mitigate the surface coking as compared to a Ni site without a Mo dopant. Our DFT-based calculations suggest that the presence of Mo-doped Ni surface site over YSZ support is thermodynamically possible and it can enhance the carbon-tolerance by increasing activation barriers for C-H bond cleavage and C-C coupling reactions compared to the Ni/YSZ catalysts. Furthermore, for the projected density of states (PDOS) of the Ni 3*d* orbital in Ni(111) with and without Mo, the *d*-band center of the Ni atom located in close proximity of the Mo atom shifts away from the Fermi level and as a result, it decreased the electronic interaction between carbon and Ni. Consequently, there would be less adsorbed carbon in the Ni-Mo system.

AUTHOR INFORMATION

Corresponding Authors

*Tel: +1 631 632 8433 Fax: +1 631 632 6269 E-mail: taejin.kim@stonybrook.edu (T. Kim)

*Tel: +1 509 335 3786 Fax: +1 509 335 4806 E-mail: suha@wsu.edu (S. Ha)

Author Contributions

The manuscript was written through contributions of all authors. All authors have given approval to the final version of the manuscript. ‡These authors contributed equally.

ACKNOWLEDGMENTS

This experimental work at WSU was financially supported by the Office of Naval Research (Grant No. N00014-15-1-2416). The computational work was primarily funded by the U.S. Department of Energy, Office of Basic Energy Sciences, Division of Chemical Sciences, Biosciences within the Catalysis Science program, under award number DE-SC0014560. This work was partially funded by the Joint Center for Deployment and Research in Earth Abundant Materials (JCDREAM) in Washington State. We also thank the Franceschi Microscopy and Imaging Center at Washington State University for use of their facilities. This research used resources from the Center for Institutional Research Computing at Washington State University. PNNL is a multi-program national laboratory operated for the U.S. DOE by Battelle. T. Kim gratefully acknowledge the financial support from Stony Brook University (SBU) and Brookhaven National Lab (BNL) (Grant # 37298), as well as Center for Functional Nanomaterials at BNL, which is supported by

the U.S. Department of Energy, Office of Basic Energy Sciences, under Contract No. DE-SC0012704.

SUPPLEMENTARY DATA

Supplementary data associated with this article can be found in the online version.

REFERENCES

(1) Biloen, P.; Sachtler, W. M. H. Mechanism of Hydrocarbon Synthesis over Fischer-Tropsch Catalysts. *Adv. Catal.* **1981**, *30* (C), 165–216. https://doi.org/10.1016/S0360-0564(08)60328-4.

(2) Shah, S.; Marin-Flores, O. G.; Chinnathambi, K.; Norton, M. G.; Ha, S. Partial Oxidation of Surrogate Jet-A Fuel over SiO_2 Supported MoO_2. *Appl. Catal. B Environ.* **2016**, *193*, 133–140. https://doi.org/10.1016/j.apcatb.2016.03.064.

(3) Kirubakaran, A.; Jain, S.; Nema, R. K. A Review on Fuel Cell Technologies and Power Electronic Interface. *Renewable and Sustainable Energy Reviews*. **2009**, pp 2430–2440. https://doi.org/10.1016/j.rser.2009.04.004.

(4) Zhao, K.; Xiaoxue H.; Qusay B., Norton M.G.; Ha, S. NiMo-Ceria-Zirconia Catalytic Reforming Layer for Solid Oxide Fuel Cells Running on a Gasoline Surrogate. *Appl. Catal. B-Environmental* **2017**, *224*, 500–507.

(5) Minh, N. Q. Solid Oxide Fuel Cell Technology - Features and Applications. *Solid State Ionics*. **2004**, 174(1-4), pp 271–277. https://doi.org/10.1016/j.ssi.2004.07.042.

(6) Kim, H.; Park, S.; Vohs, J. M.; Gorte, R. J. Direct Oxidation of Liquid Fuels in a Solid Oxide Fuel Cell. *J. Electrochem. Soc.* **2001**, *148* (7), A693. https://doi.org/10.1149/1.1374216.

(7) Hibino, T. A Low-Operating-Temperature Solid Oxide Fuel Cell in Hydrocarbon-Air Mixtures. *Science.* **2000**, *288* (5473), 2031–2033. https://doi.org/10.1126/science.288.5473.2031.

(8) Park, G. G.; Yim, S. D.; Yoon, Y. G.; Kim, C. S.; Seo, D. J.; Eguchi, K. Hydrogen Production with Integrated Microchannel Fuel Processor Using Methanol for Portable Fuel Cell Systems. *Catal. Today* **2005**, *110* (1–2), 108–113. https://doi.org/10.1016/j.cattod.2005.09.016.

(9) Mogensen, D.; Grunwaldt, J. D.; Hendriksen, P. V.; Dam-Johansen, K.; Nielsen, J. U. Internal Steam Reforming in Solid Oxide Fuel Cells: Status and Opportunities of Kinetic Studies and Their Impact on Modelling. *J. Power Sources* **2011**, *196* (1), 25–38. https://doi.org/10.1016/j.jpowsour.2010.06.091.

(10) Shekhawat, D.; Gardner, T. H.; Berry, D. A.; Salazar, M.; Haynes, D. J.; Spivey, J. J. Catalytic Partial Oxidation of N-Tetradecane in the Presence of Sulfur or Polynuclear Aromatics: Effects of Support and Metal. *Appl. Catal. A Gen.* **2006**, *311* (1–2), 8–16. https://doi.org/10.1016/j.apcata.2006.05.042.

(11) Zheng, J.; Strohm, J. J.; Song, C. Steam Reforming of Liquid Hydrocarbon Fuels for Micro-Fuel Cells. Pre-Reforming of Model Jet Fuels over Supported Metal Catalysts. *Fuel Process. Technol.* **2008**, *89* (4), 440–448. https://doi.org/10.1016/j.fuproc.2007.11.024.

(12) Lu, Y.; Jinchun C.; Ye L.; Qingsong X.; Mingyuan. H. Highly Sulfur-Tolerant $Pt/Ce_{0.8}Gd_{0.2}O_{1.9}$ Catalyst for Steam Reforming of Liquid Hydrocarbons in Fuel Cell Applications. *J. Catal.* **2008**, *254* (1), 39–48.

(13) Xie, C.; Chen, Y.; Engelhard, M. H.; Song, C. Comparative Study on the Sulfur Tolerance and Carbon Resistance of Supported Noble Metal Catalysts in Steam Reforming of Liquid Hydrocarbon Fuel. *ACS Catal.* **2012**, *2* (6), 1127–1137. https://doi.org/10.1021/cs200695t.

(14) González-Gil, R.; Chamorro-Burgos, I.; Herrera, C.; Larrubia, M. A.; Laborde, M.; Mariño, F.; Alemany, L. J. Production of Hydrogen by Catalytic Steam Reforming of Oxygenated Model Compounds on Ni-Modified Supported Catalysts. Simulation and Experimental Study. *Int. J. Hydrogen Energy* **2015**, *40* (34), 11217–11227. https://doi.org/10.1016/j.ijhydene.2015.05.167.

(15) Trane, R.; Dahl, S.; Skjøth-Rasmussen, M. S.; Jensen, A. D. Catalytic Steam Reforming of Bio-Oil. *Int. J. Hydrogen Energy* **2012**, *37* (8), 6447–6472. https://doi.org/10.1016/j.ijhydene.2012.01.023.

(16) Montero, C.; Ochoa, A.; Castaño, P.; Bilbao, J.; Gayubo, A. G. Monitoring Ni^0 and Coke Evolution during the Deactivation of a Ni/La_2O_3-α-Al_2O_3 Catalyst in Ethanol Steam Reforming in a Fluidized Bed. *J. Catal.* **2015**, *331*, 181–192. https://doi.org/10.1016/j.jcat.2015.08.005.

(17) Park, S. Y.; Gunung O.; Kwangyul K.; Myung Won Seo, Ho Won Ra, Tae Young Mun, Jae Goo Lee, and S. J. Y. Deactivation Characteristics of Ni and Ru Catalysts in Tar Steam Reforming. *Renew. Energy* **2017**, *105*, 76–83.

(18) Bkour, Q.; Marin-Flores, O. G.; Graham, T. R.; Ziaei, P.; Saunders, S. R.; Norton, M. G.; Ha, S. Nickel Nanoparticles Supported on Silica for the Partial Oxidation of Isooctane. *Appl. Catal. A Gen.* **2017**, *546*, 126–135. https://doi.org/10.1016/j.apcata.2017.08.015.

(19) Li, L.; He, S.; Song, Y.; Zhao, J.; Ji, W.; Au, C. T. Fine-Tunable Ni@porous Silica Core-Shell Nanocatalysts: Synthesis, Characterization, and Catalytic Properties in Partial Oxidation of Methane to Syngas. *J. Catal.* **2012**, *288*, 54–64. https://doi.org/10.1016/j.jcat.2012.01.004.

(20) Kim, J.-H.; Suh, D. J.; Park, T.-J.; Kim, K.-L. Effect of Metal Particle Size on Coking during CO2 Reforming of CH4 over Ni–Alumina Aerogel Catalysts. *Appl. Catal. A Gen.* **2000**, *197* (2), 191–200. https://doi.org/10.1016/S0926-860X(99)00487-1.

(21) Li, S.; Zhang, C.; Huang, Z.; Wu, G.; Gong, J. A Ni@ZrO $_2$ Nanocomposite for Ethanol Steam Reforming: Enhanced Stability via Strong Metal–Oxide Interaction. *Chem. Commun.* **2013**, *49* (39), 4226–4228. https://doi.org/10.1039/C2CC37109J.

(22) Zhang, C.; Zhu, W.; Li, S.; Wu, G.; Ma, X.; Wang, X.; Gong, J. Sintering-Resistant Ni-Based Reforming Catalysts Obtained via the Nanoconfinement Effect. *Chem. Commun.* **2013**, *49* (82), 9383. https://doi.org/10.1039/c3cc43895c.

(23) Li, S.; Gong, J.; Ferreira-Aparicio, P.; Benito, M. J.; Sanz, J. L.; McFarland, E.; Huber, G. W.; Shabaker, J. W.; Dumesic, J. A.; Mattos, L. V.; et al. Strategies for Improving the Performance and Stability of Ni-Based Catalysts for Reforming Reactions. *Chem. Soc. Rev.* **2014**, *43* (21), 7245–7256. https://doi.org/10.1039/C4CS00223G.

(24) Wolfbeisser, A.; Sophiphun, O.; Bernardi, J.; Wittayakun, J.; Föttinger, K.; Rupprechter, G. Methane Dry Reforming over Ceria-Zirconia Supported Ni Catalysts. *Catalysis Today*.

2016, 227, 234-245. https://doi.org/10.1016/j.cattod.2016.04.025.

(25) Moretti, E.; Storaro, L.; Talon, A.; Chitsazan, S.; Garbarino, G.; Busca, G.; Finocchio, E. Ceria-Zirconia Based Catalysts for Ethanol Steam Reforming. *Fuel* **2015**, *153*, 166–175. https://doi.org/10.1016/j.fuel.2015.02.077.

(26) Bkour Q; Zhao K; Scudiero L; Yoon CW, Marin-Flores OG, Norton MG, H. S. Synthesis and Performance of Ceria-Zirconia Supported Ni-Mo Nanoparticles for Partial Oxidation of Isooctane. *Appl. Catal. B Environ.* **2017**, *212*, 97–105.

(27) Ishihara, T.; Yan, J.; Shinagawa, M.; Matsumoto, H. Ni-Fe Bimetallic Anode as an Active Anode for Intermediate Temperature SOFC Using $LaGaO_3$ Based Electrolyte Film. *Electrochim. Acta* **2006**, *52* (4), 1645–1650. https://doi.org/10.1016/j.electacta.2006.03.103.

(28) Kim, H.; Lu, C.; Worrell, W. L.; Vohs, J. M.; Gorte, R. J. Cu-Ni Cermet Anodes for Direct Oxidation of Methane in Solid-Oxide Fuel Cells. *J. Electrochem. Soc.* **2002**, *149* (3), A247. https://doi.org/10.1149/1.1445170.

(29) Kan, H.; Hyun, S. H.; Shul, Y. G.; Lee, H. Improved Solid Oxide Fuel Cell Anodes for the Direct Utilization of Methane Using Sn-Doped Ni/YSZ Catalysts. *Catal. Commun.* **2009**, *11* (3), 180–183. https://doi.org/10.1016/j.catcom.2009.09.021.

(30) An, W.; Gatewood, D.; Dunlap, B.; Turner, C. H. Catalytic Activity of Bimetallic Nickel Alloys for Solid-Oxide Fuel Cell Anode Reactions from Density-Functional Theory. *J. Power Sources* **2011**, *196*, 4724–4728.

(31) Nikolla, E.; Holewinski, A.; Schwank, J.; Linic, S. Controlling Carbon Surface Chemistry by Alloying: Carbon Tolerant Reforming Catalyst. *J. Am. Chem. Soc.* **2006**, *128* (35), 11354–11355. https://doi.org/10.1021/ja0638298.

(32) Nikolla, E.; Schwank, J.; Linic, S. Promotion of the Long-Term Stability of Reforming Ni Catalysts by Surface Alloying. *J. Catal.* **2007**, *250* (1), 85–93. https://doi.org/10.1016/j.jcat.2007.04.020.

(33) Nikolla, E.; Schwank, J. W.; Linic, S. Hydrocarbon Steam Reforming on Ni Alloys at Solid Oxide Fuel Cell Operating Conditions. *Catal. Today* **2008**, *136* (3–4), 243–248. https://doi.org/10.1016/j.cattod.2008.03.028.

(34) Bkour, Q.; Marin-Flores, O. G.; Norton, M. G.; Ha, S. A Highly Active and Stable Bimetallic Ni-Mo2C Catalyst for a Partial Oxidation of Jet Fuel. *Appl. Catal. B Environ.* **2019**, *245*, 613–622. https://doi.org/10.1016/j.apcatb.2019.01.027.

(35) Shah, S.; Marin-Flores, O. G.; Norton, M. G.; Ha, S. Molybdenum Carbide Supported Nickel-Molybdenum Alloys for Synthesis Gas Production via Partial Oxidation of Surrogate Biodiesel. *J. Power Sources* **2015**, *294*, 530–536. https://doi.org/10.1016/j.jpowsour.2015.06.075.

(36) Quincoces, C. E.; De Vargas, S. P.; Grange, P.; González, M. G. Role of Mo in CO2 Reforming of CH4 over Mo Promoted Ni/Al2O3 Catalysts. *Mater. Lett.* **2002**, *56* (5), 698–704. https://doi.org/10.1016/S0167-577X(02)00598-0.

(37) González, M. G.; Ponzi, E. N.; Ferretti, O. A.; Quincoces, C. E.; Marecot, P.; Barbier, J. Studies on H_2S Adsorption and Carbon Deposition over Mo-Ni/Al_2O_3 Catalysts. *Adsorpt. Sci. Technol.* **2000**, 18.6, 541-550. https://doi.org/10.1260/0263617001493602.

(38) Zhan, Z.; Barnett, S. A. Solid Oxide Fuel Cells Operated by Internal Partial Oxidation Reforming of Iso-Octane. *J. Power Sources* **2006**, *155* (2), 353–357. https://doi.org/10.1016/j.jpowsour.2005.04.015.

(39) Bae, G.; Bae, J.; Kim-Lohsoontorn, P.; Jeong, J. Performance of SOFC Coupled with N-C_4H_{10} Autothermal Reformer: Carbon Deposition and Development of Anode Structure. *Int. J. Hydrogen Energy* **2010**, *35* (22), 12346–12358. https://doi.org/10.1016/j.ijhydene.2010.08.125.

(40) Zhao, K. and Du, Y. Calcium-Doped Ceria Materials for Anode of Solid Oxide Fuel Cells Running on Methane Fuel. *J. Power Sources* **2017**, *347*, 79–85.

(41) Zhao, K.; Hou, X.; Bkour, Q.; Norton, M. G.; Ha, S. NiMo-Ceria-Zirconia Catalytic Reforming Layer for Solid Oxide Fuel Cells Running on a Gasoline Surrogate. *Appl. Catal. B Environ.* **2018**, *224*, 500–507. https://doi.org/10.1016/j.apcatb.2017.10.067.

(42) Kresse, G.; Hafner, J. Ab Initio Molecular Dynamics for Liquid Metals. *Phys. Rev. B* **1993**, *47* (1), 558–561. https://doi.org/10.1103/PhysRevB.47.558.

(43) Kresse, G.; Furthmüller, J. Efficiency of Ab-Initio Total Energy Calculations for Metals and Semiconductors Using a Plane Wave Basis Set. *Comput. Mat. Sci.* **1996**, *6* (1), 15–50.

(44) Perdew, J. P.; Ernzerhof, M.; Burke, K. Generalized Gradient Approximation Made Simple. *Phys. Rev. Lett.* **1996**, *77*, 3865–3868. https://doi.org/10.1103/PhysRevLett.77.3865.

(45) Payne M. C.; Teter, M. P.; Allan, D. C.; Arias, T. A.; Joannopoulos, J. D. Iterative Minization Techniques for Ab Initio Total-Energy Calculations: Molecular Dynamics and Conjugate Gradient. *Rev. Mod. Phys.* **1992**, *64* (4), 1045–1097. https://doi.org/10.1103/RevModPhys.64.1045.

(46) Lejaeghere, K.; Bihlmayer, G.; Björkman, T.; Blaha, P.; Blügel, S.; Blum, V.; Caliste, D.; Castelli, I. E.; Clark, S. J.; Dal Corso, A.; et al. Reproducibility in Density Functional Theory Calculations of Solids. *Science*, **2016**, 351(6280), aad3000. https://doi.org/10.1126/science.aad3000.

(47) Shishkin, M.; Ziegler, T. Oxidation of H 2 , CH 4 , and CO Molecules at the Interface between Nickel and Yttria-Stabilized Zirconia: A Theoretical Study Based on DFT. *J. Phys. Chem. C* **2009**, *113* (52), 21667–21678. https://doi.org/10.1021/jp905615c.

(48) Shishkin, M.; Ziegler, T. The Electronic Structure and Chemical Properties of a Ni/CeO 2 Anode in a Solid Oxide Fuel Cell: A DFT + U Study. *J. Phys. Chem. C* **2010**, *114*, 21411–21416. https://doi.org/10.1021/jp105316p.

(49) Shishkin, M.; Ziegler, T. Hydrogen Oxidation at the Ni/Yttria-Stabilized Zirconia Interface: A Study Based on Density Functional Theory. *J. Phys. Chem. C* **2010**, *114* (25), 11209–11214. https://doi.org/10.1021/jp1030575.

(50) Shishkin, M.; Ziegler, T. Direct Modeling of the Electrochemistry in the Three-Phase Boundary of Solid Oxide Fuel Cell Anodes by Density Functional Theory: A Critical Overview. *Phys. Chem. Chem. Phys.* **2014**, *16* (5), 1798–1808. https://doi.org/10.1039/c3cp53943a.

(51) Monkhorst, H.; Pack, J. Special Points for Brillouin Zone Integrations. *Phys. Rev. B* **1976**, *13* (12), 5188–5192. https://doi.org/10.1103/PhysRevB.13.5188.

(52) Che, F.; Hensley, A. J.; Ha, S.; McEwen, J. S. Decomposition of Methyl Species on a Ni(211) Surface: Investigations of the Electric Field Influence. *Catal. Sci. Technol.* **2014**, *4* (11), 4020–4035. https://doi.org/10.1039/c4cy00406j.

(53) Che, F.; Gray, J. T.; Ha, S.; McEwen, J. S. Catalytic Water Dehydrogenation and Formation on Nickel: Dual Path Mechanism in High Electric Fields. *J. Catal.* **2015**, *332*, 187–200. https://doi.org/10.1016/j.jcat.2015.09.010.

(54) Che, F.; Ha, S.; McEwen, J.-S. Elucidating the Field Influence on the Energetics of the Methane Steam Reforming Reaction: A Density Functional Theory Study. *Appl. Catal. B Environ.* **2016**, *195*, 77–89. https://doi.org/10.1016/j.apcatb.2016.04.026.

(55) Che, F.; Ha, S.; McEwen, J. S. Elucidating the Role of the Electric Field at the Ni/YSZ Electrode: A DFT Study. *J. Phys. Chem. C* **2016**, *120* (27), 14608–14620. https://doi.org/10.1021/acs.jpcc.6b01292.

(56) Che, F.; Ha, S.; McEwen, J. S. Catalytic Reaction Rates Controlled by Metal Oxidation State: C−H Bond Cleavage in Methane over Nickel-Based Catalysts. *Angew. Chemie - Int. Ed.* **2017**, *56* (13), 3557–3561. https://doi.org/10.1002/anie.201611796.

(57) Montoya, J. A.; Romero-Pascual, E.; Gimon, C.; Del Angel, P.; Monzón, A. Methane Reforming with CO_2 over Ni/ZrO_2–CeO_2 Catalysts Prepared by Sol–Gel. *Catal. Today* **2000**, *63* (1), 71–85. https://doi.org/10.1016/S0920-5861(00)00447-8.

(58) Borowiecki, T.; Golebiowski, A.; Stasinska, B. Effects of Small MoO3 Additions on the Properties of Nickel Catalysts for the Steam Reforming of Hydrocarbons. *Appl. Catal. A Gen.* **1997**, *153* (1–2), 141–156. https://doi.org/10.1016/S0926-860X(01)00997-8.

(59) Qi, W.; Chen, S.; Wu, Y.; Xie, K. A Chromium Oxide Coated Nickel/Yttria Stabilized Zirconia Electrode with a Heterojunction Indftterface for Use in Electrochemical Methane Reforming. *RSC Adv.* **2015**, *5* (59), 47599–47608. https://doi.org/10.1039/C5RA01927C.

(60) Abo-Zeid, M. M.; El-Deab, M. S.; Abdel Kareem, A.; El-Kady, O. A. M.; Daher, A. M. Impurities Effect on the Charge Mobility of Yttria-Stabilized Zirconia. Int. J. Electrochem. Sci. **2016**, 11 (2016): 3137-3146. https://doi.org/10.20964/110403137.

(61) Hartmann, M.; Maier, L.; Minh, H. D.; Deutschmann, O. Catalytic Partial Oxidation of Iso-Octane over Rhodium Catalysts: An Experimental, Modeling, and Simulation Study. *Combust. Flame* **2010**, *157* (9), 1771–1782. https://doi.org/10.1016/j.combustflame.2010.03.005.

(62) Pengpanich, S.; Meeyoo, V.; Rirksomboon, T.; Schwank, J. Iso-Octane Partial Oxidation over $Ni\text{-}Sn/Ce_{0.75}Zr_{0.25}O_2$ Catalysts. *Catal. Today* **2008**, *136* (3–4), 214–221. https://doi.org/10.1016/j.cattod.2008.01.018.

(63) Marin Flores, O. G.; Ha, S. Activity and Stability Studies of MoO2 Catalyst for the Partial Oxidation of Gasoline. *Appl. Catal. A Gen.* **2009**, *352* (1–2), 124–132. https://doi.org/10.1016/j.apcata.2008.09.036.

(64) Huang, T.; Huang, W.; Huang, J.; Ji, P. Methane Reforming Reaction with Carbon Dioxide over SBA-15 Supported Ni-Mo Bimetallic Catalysts. *Fuel Process. Technol.* **2011**, *92* (10), 1868–1875. https://doi.org/10.1016/j.fuproc.2011.05.002.

(65) Baker, R. Catalytic Growth of Carbon Filaments☆. *Carbon N. Y.* **1989**, *27* (3), 315–323. https://doi.org/10.1016/0008-6223(89)90062-6.

(66) Sugisawa, M.; Takanabe, K.; Harada, M.; Kubota, J.; Domen, K. Effects of La Addition to Ni/Al_2O_3 Catalysts on Rates and Carbon Deposition during Steam Reforming of n-Dodecane. *Fuel Process. Technol.* **2011**, *92* (1), 21–25. https://doi.org/10.1016/j.fuproc.2010.08.014.

(67) Shabaker, J. W.; Simonetti, D. A.; Cortright, R. D.; Dumesic, J. A. Sn-Modified Ni Catalysts for Aqueous-Phase Reforming: Characterization and Deactivation Studies. *J. Catal.* **2005**, 231(1), 67-76. https://doi.org/10.1016/j.jcat.2005.01.019.

(68) Boot, M. D.; Tian, M.; Hensen, E. J. M.; Mani Sarathy, S. Impact of Fuel Molecular Structure on Auto-Ignition Behavior – Design Rules for Future High Performance Gasolines. *Progress in Energy and Combustion Science*. **2017**, 60, 1-25. https://doi.org/10.1016/j.pecs.2016.12.001.

(69) Coq, B.; Figueras, F. Bimetallic Palladium Catalysts: Influence of the Co-Metal on the Catalyst Performance. *J. Mol. Catal. A Chem.* **2001**, *173* (1–2), 117–134. https://doi.org/10.1016/S1381-1169(01)00148-0.

(70) Liu, Z.; Zhou, J.; Cao, K.; Yang, W.; Gao, H.; Wang, Y.; Li, H. Highly Dispersed Nickel Loaded on Mesoporous Silica: One-Spot Synthesis Strategy and High Performance as Catalysts for Methane Reforming with Carbon Dioxide. *Appl. Catal. B Environ.* **2012**, *125*, 324–330. https://doi.org/10.1016/j.apcatb.2012.06.003.

(71) Arslan, A.; Gunduz, S.; Dogu, T. Steam Reforming of Ethanol with Zirconia Incorporated Mesoporous Silicate Supported Catalysts. *Int. J. Hydrogen Energy* **2014**, *39* (32), 18264–18272. https://doi.org/10.1016/j.ijhydene.2014.09.030.

(72) Rocha, R. A.; Muccillo, E. N. S.; Dessemond, L.; Djurado, E. Thermal Ageing of Nanostructured Tetragonal Zirconia Ceramics: Characterization of Interfaces. *J. Eur. Ceram. Soc.* **2010**. https://doi.org/10.1016/j.jeurceramsoc.2009.05.004.

(73) Xie, S.; Iglesia, E.; Bell, A. T. Water-Assisted Tetragonal-to-Monoclinic Phase Transformation of ZrO_2 at Low Temperatures. *Chem. Mater.* **2000**. 12(8), 2442-2447. https://doi.org/10.1021/cm000212v.

(74) Bañares, M. A.; Wachs, I. E. Molecular Structures of Supported Metal Oxide Catalysts under Different Environments. *J. Raman Spectrosc.* **2002**, 33(5), 359-380. https://doi.org/10.1002/jrs.866.

(75) Hu, H.; Wachs, I. E. Surface Structures of Supported Molybdenum Oxide Catalysts.

Characterization by Raman and Mo L3-Edge XANES. *J. Phys. Chem.* **1995**, 99(27), 10897-10910. https://doi.org/10.1021/j100027a034.

(76) Rochet, A.; Baubet, B.; Moizan, V.; Devers, E.; Hugon, A.; Pichon, C.; Payen, E.; Briois, V. Influence of the Preparation Conditions of Oxidic $NiMo/Al_2O_3$ Catalysts on the Sulfidation Ability: A Quick-XAS and Raman Spectroscopic Study. *J. Phys. Chem. C* **2015**, 119(42), 23928-23942. https://doi.org/10.1021/acs.jpcc.5b06219.

(77) Wachs, I. E.; Roberts, C. A. Monitoring Surface Metal Oxide Catalytic Active Sites with Raman Spectroscopy. *Chemical Society Reviews*. **2010**, 39(12), 5002-5017. https://doi.org/10.1039/c0cs00145g.

(78) Tian, H.; Wachs, I. E.; Briand, L. E. Comparison of UV and Visible Raman Spectroscopy of Bulk Metal Molybdate and Metal Vanadate Catalysts. *J. Phys. Chem. B* **2005**. https://doi.org/10.1021/jp053879j.

(79) Tian, H.; Roberts, C. A.; Wachs, I. E. Molecular Structural Determination of Molybdena in Different Environments: Aqueous Solutions, Bulk Mixed Oxides, and Supported MoO3catalysts. *J. Phys. Chem. C* **2010**. https://doi.org/10.1021/jp103269w.

(80) Kalampounias, A. G.; Tsilomelekis, G.; Berg, R. W.; Boghosian, S. Molybdenum(VI) Oxosulfato Complexes in MoO3-K2S2O7-K2SO4molten Mixtures: Stoichiometry, Vibrational Properties, and Molecular Structures. *J. Phys. Chem. A* **2012**. 116(35), 88618872. https://doi.org/10.1021/jp306701k.

(81) Chan, S. S.; Wachs, I. E. In Situ Laser Raman Spectroscopy of Nickel Oxide Supported on γ-Al2O3. *J. Catal.* **1987**. 103(1). https://doi.org/10.1016/0021-9517(87)90112-6.

(82) Chen, B.; Zhu, Z.; Ma, J.; Yang, M.; Hong, J.; Hu, X.; Qiu, Y.; Chen, J. One-Pot, Solid-Phase Synthesis of Magnetic Multiwalled Carbon Nanotube/Iron Oxide Composites and Their Application in Arsenic Removal. *J. Colloid Interface Sci.* **2014**. 434 (2014), 9-17. https://doi.org/10.1016/j.jcis.2014.07.046.

(83) Němeček, D.; Thomas, G. J. Raman Spectroscopy of Graphene and Related Materials. In *Frontiers of Molecular Spectroscopy*; **2009**. https://doi.org/10.1016/B978-0-444-53175-9.00016-7.

(84) Marin-Flores, O.; Turba, T.; Ellefson, C.; Wang, K.; Breit, J.; Ahn, J.; Norton, M. G.; Ha, S. Nanoparticle Molybdenum Dioxide: A Highly Active Catalyst for Partial Oxidation of Aviation Fuels. *Appl. Catal. B Environ.* **2010**, *98* (3–4), 186–192. https://doi.org/10.1016/j.apcatb.2010.05.028.

(85) Katrib, A.; Sobczak, J. W.; Krawczyk, M.; Zommer, L.; Benadda, A.; Jablonski, A.; Maire, G. Surface Studies and Catalytic Properties of the Bifunctional Bulk MoO2 System. In *Surface and Interface Analysis*; **2002**, 34(1), 225-229. https://doi.org/10.1002/sia.1288.

(86) Vannice, M. A. An Analysis of the Mars-van Krevelen Rate Expression. *Catal. Today* **2007**, *123* (1–4), 18–22. https://doi.org/10.1016/j.cattod.2007.02.002.

(87) Zhao, K.; Lee, K. S.; Chen, M.; Kim, B. H.; Xu, Q.; Ahn, B. G. Electrochemical Performance of a Copper-Impregnated $Ni\text{-}Ce_{0.8}Sm_{0.2}O_{1.9}$ Anode Running on Methane.

Int. J. Hydrogen Energy **2013**, *38* (9), 3750–3756. https://doi.org/10.1016/j.ijhydene.2013.01.036.

(88) McEwen, J. S.; Anggara, T.; Schneider, W. F.; Kispersky, V. F.; Miller, J. T.; Delgass, W. N.; Ribeiro, F. H. Integrated Operando X-Ray Absorption and DFT Characterization of Cu-SSZ-13 Exchange Sites during the Selective Catalytic Reduction of NOxwith NH3. In *Catalysis Today*; **2012**; 184, 129–144. https://doi.org/10.1016/j.cattod.2011.11.037.

(89) Reuter, K.; Stampf, C.; Scheffler, M. AB Initio Atomistic Thermodynamics and Statistical Mechanics of Surface Properties and Functions. In *Handbook of Materials Modeling*; **2005**; 149–194. https://doi.org/10.1007/978-1-4020-3286-8_10.

(90) Getman, R. B.; Xu, Y.; Schneider, W. F. Thermodynamics of Environment-Dependent Oxygen Chemisorption on Pt(111). *J. Phys. Chem. C* **2008**, *112* (26), 9559–9572. https://doi.org/10.1021/jp800905a.

(91) Reuter, K.; Scheffler, M. Composition, Structure and Stability of RuO_2(110) as a Function of Oxygen Pressure. *Phys. Rev. B* **2001**, *65*, 035406. https://doi.org/10.1103/PhysRevB.65.035406.

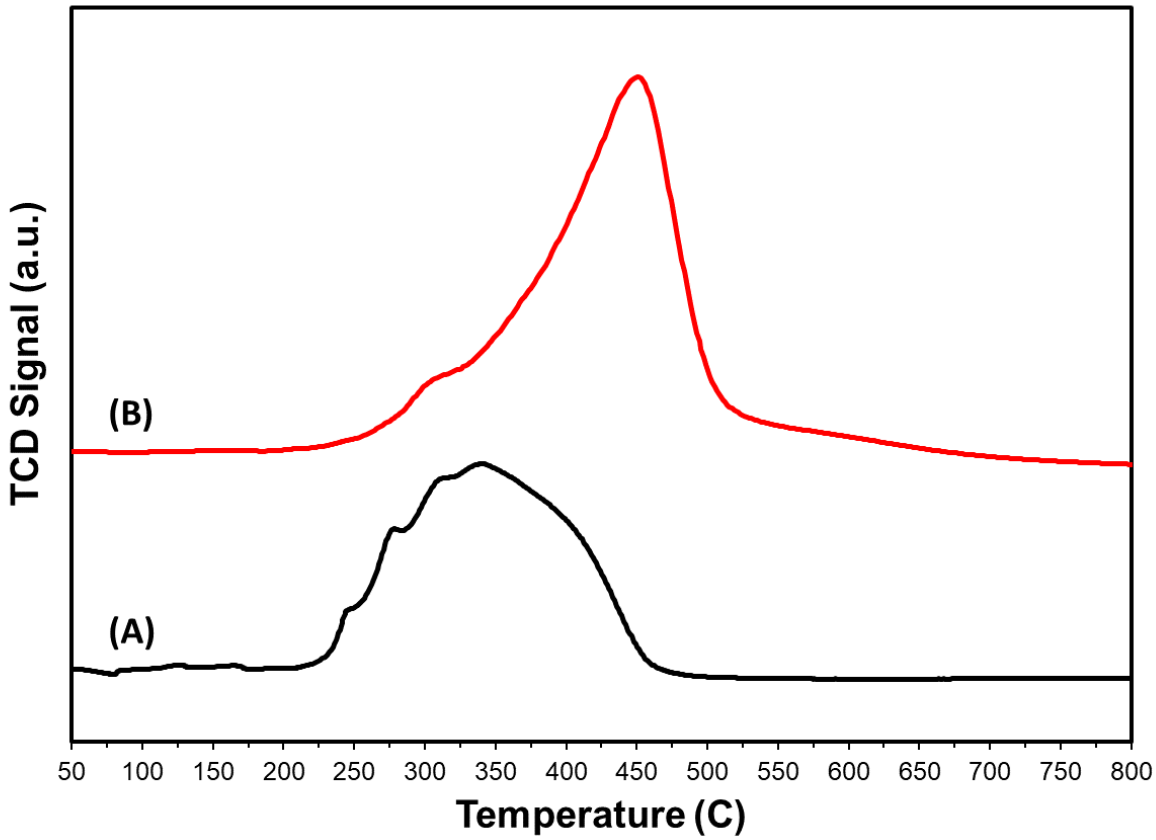

Figure 1. H_2-TPR of Ni/YSZ (A) and Ni-Mo/YSZ (B). The Ni-Mo/YSZ reduction peaks are shifted to higher temperatures, which can be related to the improvement of the metal-support interaction and enhancement of the Ni dispersion over the YSZ support after the addition of Mo species.

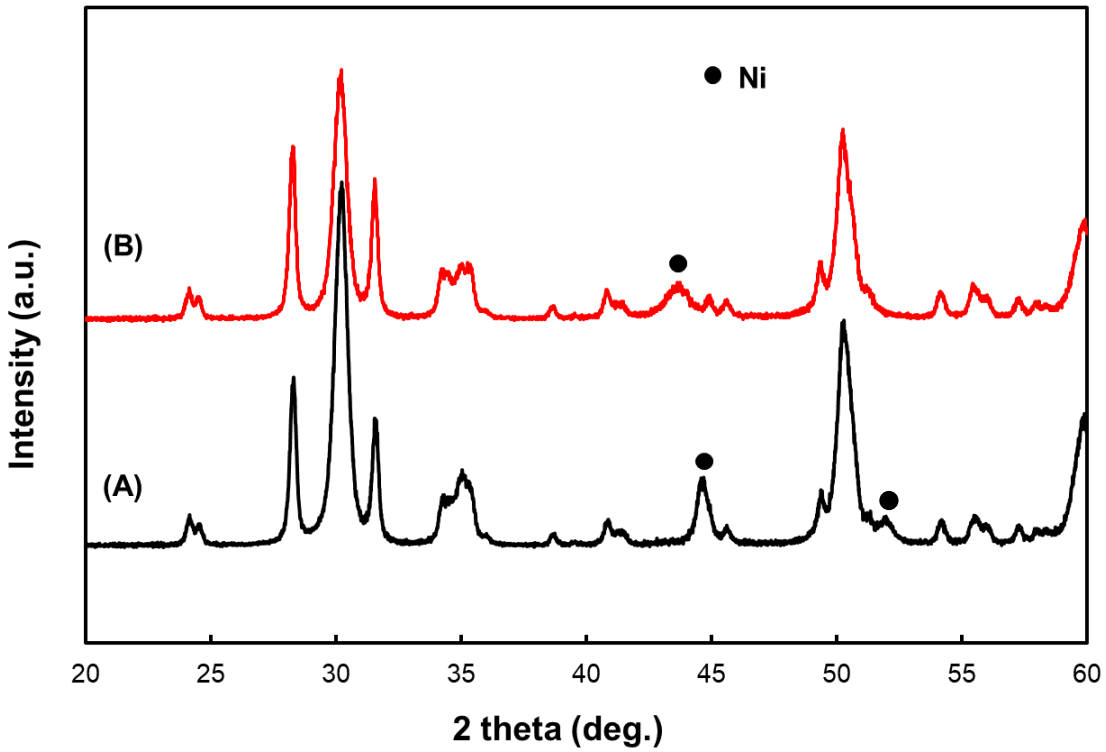

Figure 2. XRD patterns of Ni/YSZ (A) and Ni-Mo/YSZ (B). With the addition of Mo, the main diffraction peak of the Ni metal (44.5°) is shifted to a lower 2Θ value. This is attributed to the expansion of the Ni lattice due to the partial substitution of Ni atoms by larger Mo atoms during the formation of a Ni-Mo solid solution. All other non-labeled diffraction peaks correspond to YSZ.

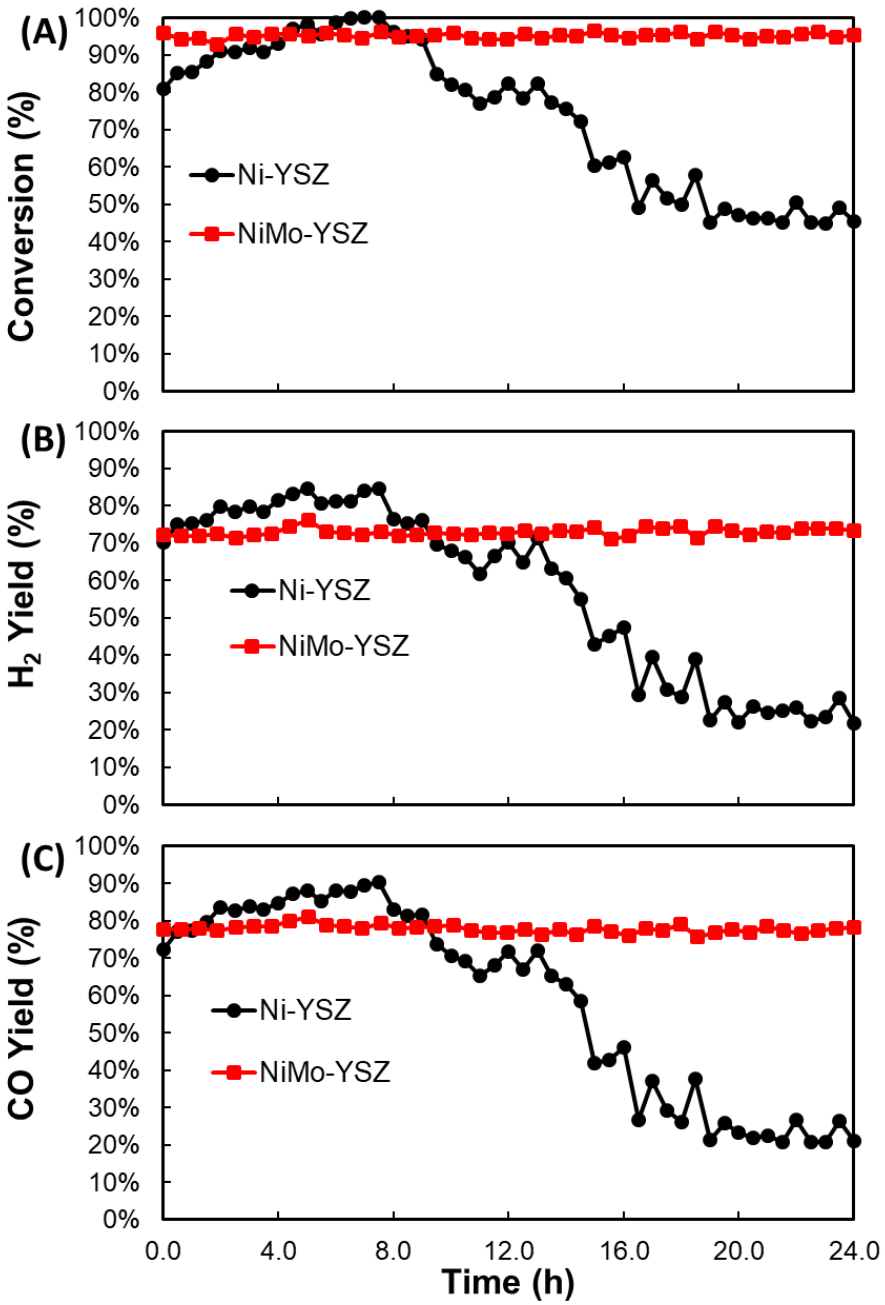

Figure 3. Isooctane conversion (A), H_2 yield (B), and CO yield (C) of the Ni/YSZ and the Ni-Mo/YSZ system. The partial oxidation reactions are performed at 750 °C, WHSV of 13.8 h^{-1}, residence time of 35 ms, catalyst mass of 0.1 g, and O_2/C ratio of 0.5. The flow rates of isooctane and air are fixed at 2 ml/h and 86 sccm, respectively.

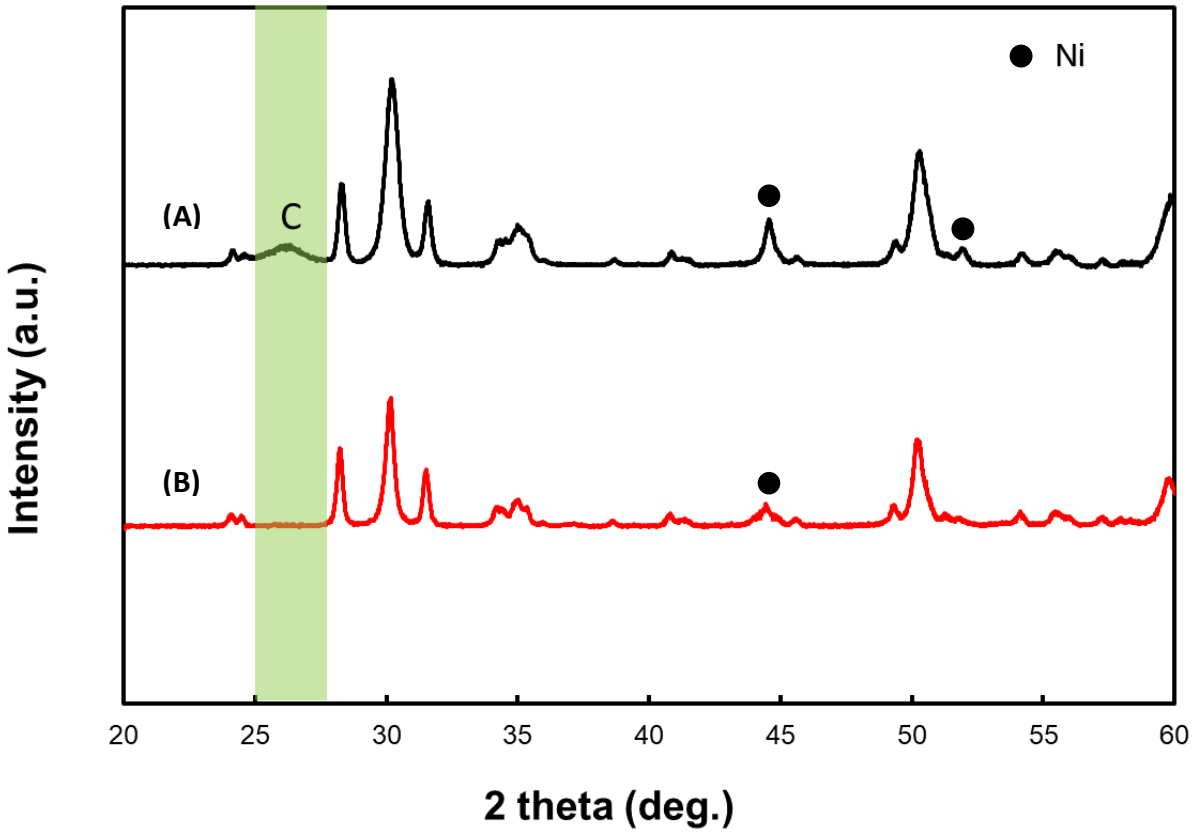

Figure 4. XRD patterns of the spent Ni/YSZ (A) and the spent Ni-Mo/YSZ (B) samples after operating them under the isooctane POX reaction for 24 hours. The Ni-Mo/YSZ spent sample shows no indication of carbon formation and it suffers much less nanoparticle aggregation during the reforming reaction than that of the Ni/YSZ sample.

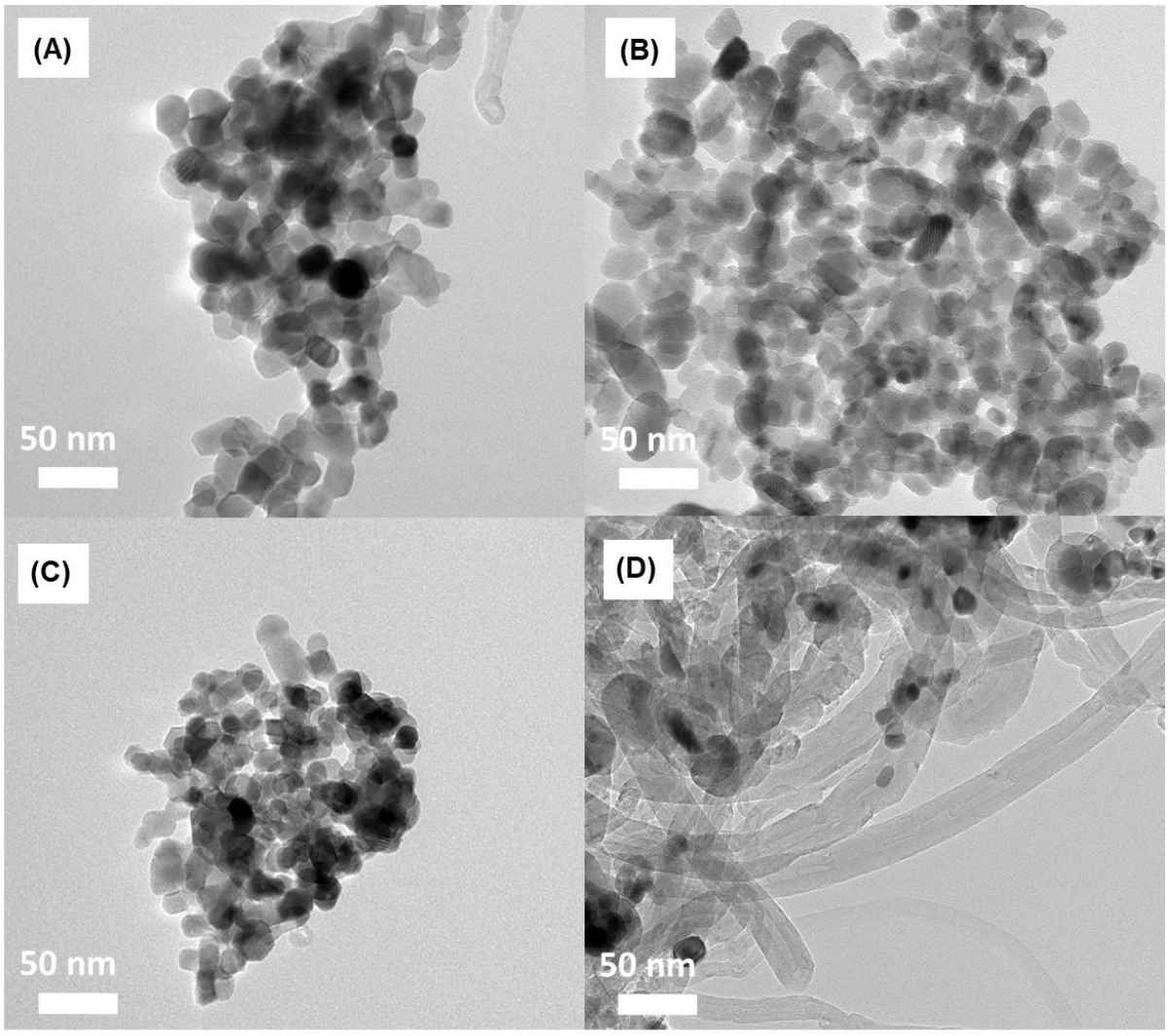

Figure 5. TEM images of the fresh Ni-Mo/YSZ (A), spent Ni-Mo/YSZ (B), fresh Ni/YSZ (C), and spent Ni/YSZ (D). For these spent samples, they are first operated under the isooctane POX reaction for 24 hours at 750 °C and WHSV of 13.8 h^{-1}. The addition of Mo to the Ni/YSZ catalyst system effectively reduces the growth of whisker carbon.

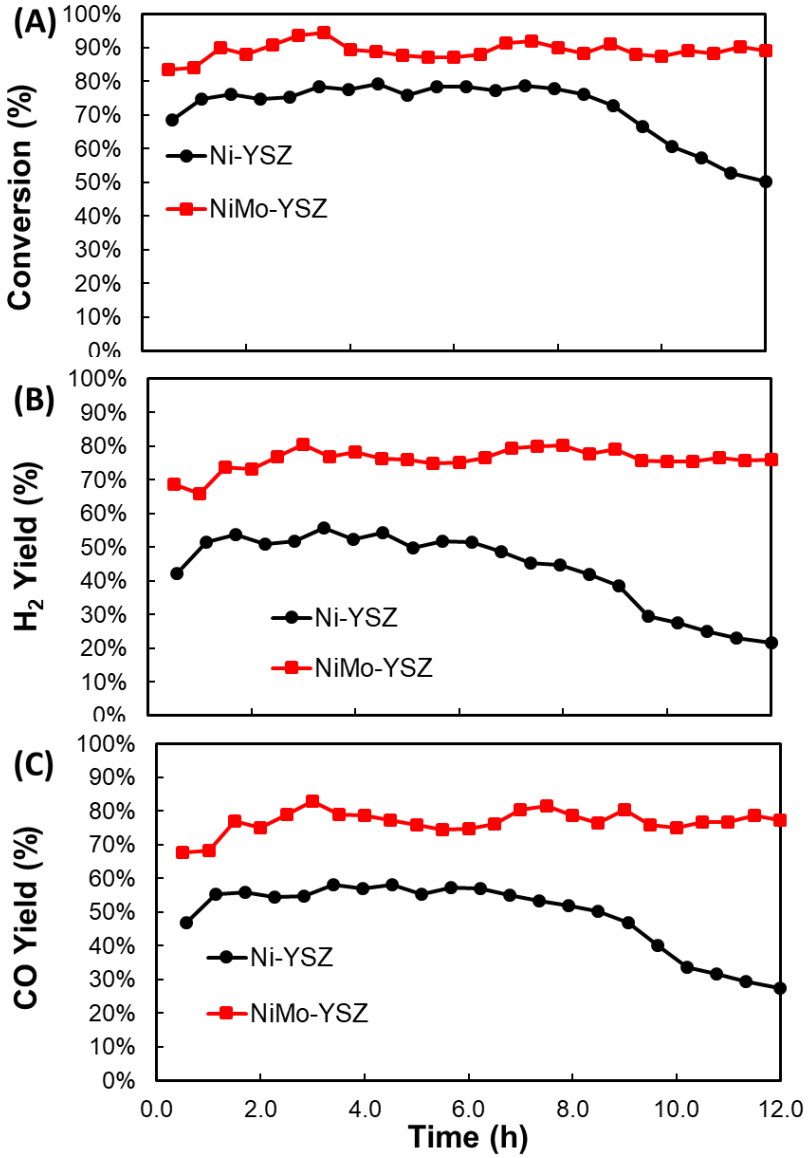

Figure 6. Gasoline conversion (A), H_2 yield (B), and CO yield (C) of the Ni/YSZ and the Ni-Mo/YSZ samples. The partial oxidation reactions are performed at 750 °C, WHSV of 13.8 h^{-1}, residence time of 35 ms, catalyst mass of 0.1 g, and O_2/C ratio of 0.5. The flow rates of isooctane and air are fixed at 2 ml/h and 86 sccm, receptively. Gasoline is purchased from our local gas station in Pullman, WA, USA.

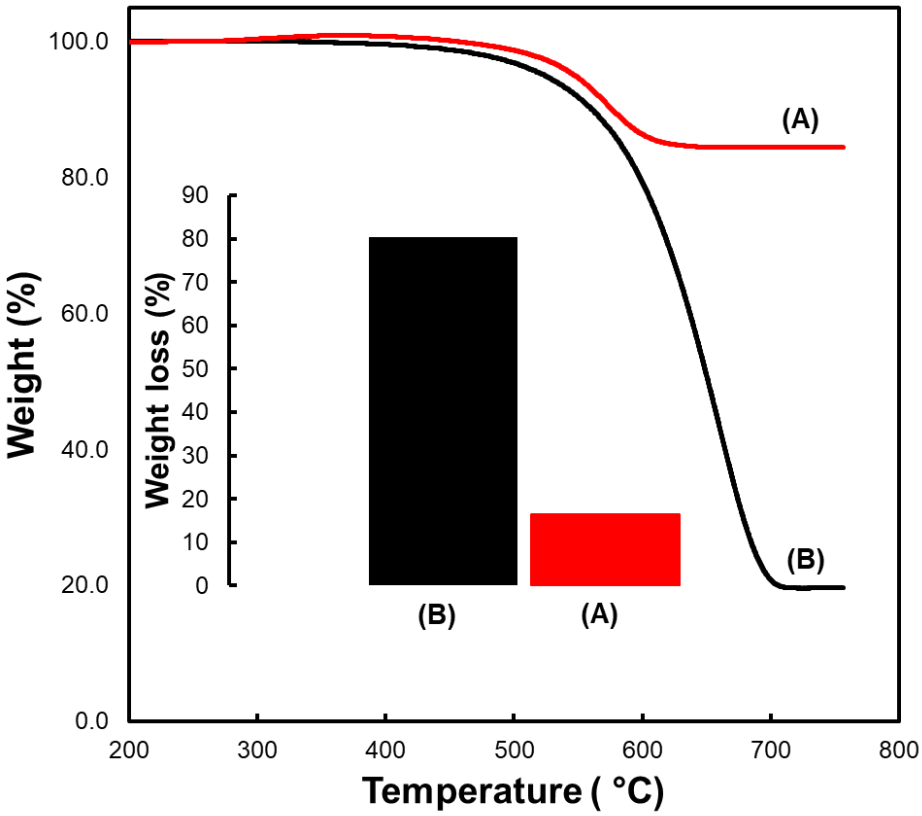

Figure 7. TGA profiles of Ni-Mo/YSZ (A) and Ni/YSZ (B) after 12 h of gasoline POX test (750 °C, WHSV of 13.8 h^{-1}, and O_2/C of 0.5). The Ni/YSZ sample shows much higher weight loss (~80 wt.%) indicating a much larger amount of coke formation compared to that of Ni-Mo/YSZ sample (~17 wt.%).

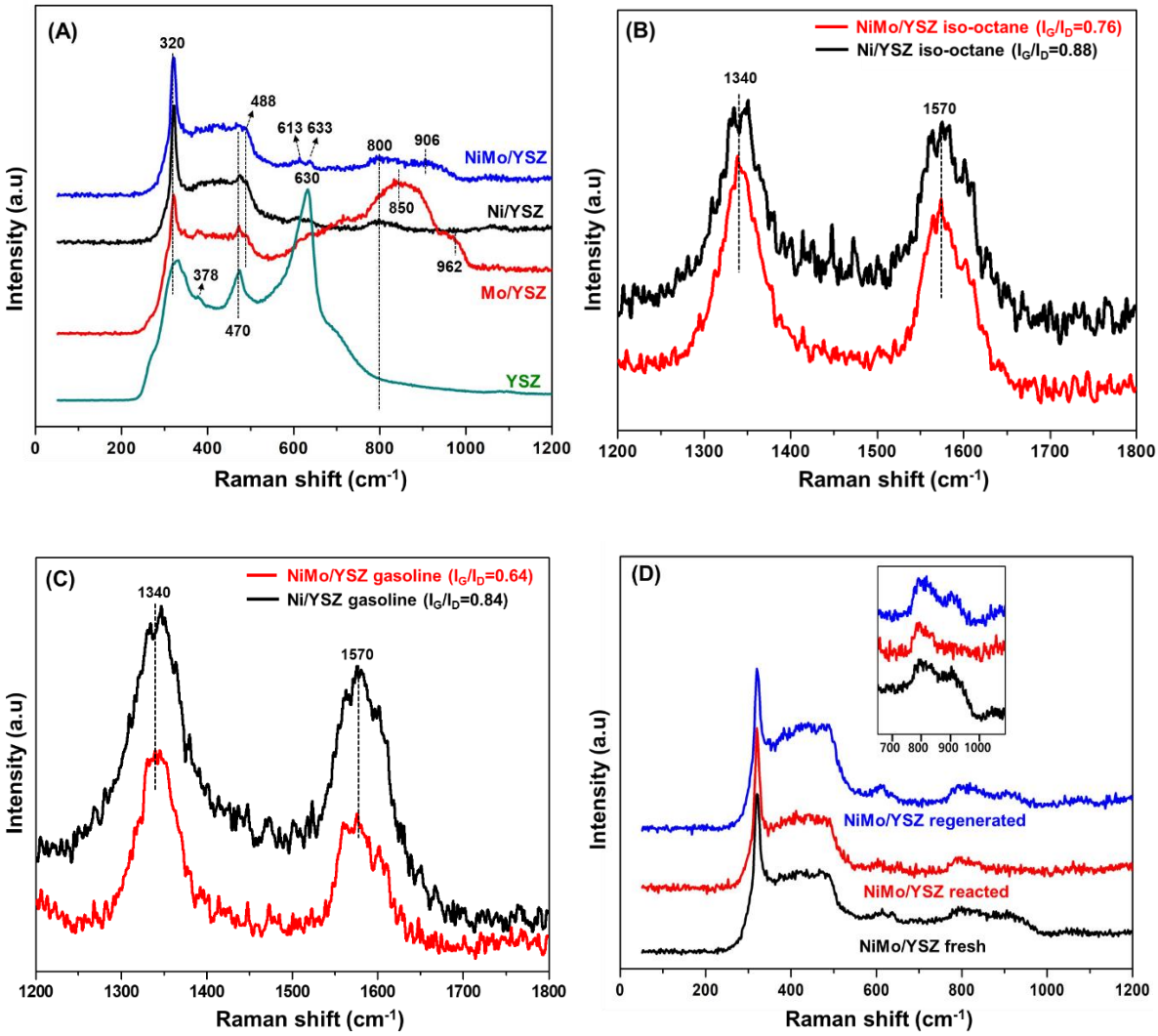

Figure 8. UV-Raman spectra of (A) the YSZ and fresh YSZ supported Ni, Mo, and Ni-Mo catalysts, Visible-Raman spectra of (B) iso-octane reacted Ni/YSZ and Ni-Mo/YSZ catalysts, Visible-Raman spectra of (C) gasoline reacted Ni/YSZ and Ni-Mo/YSZ catalysts, UV-Raman spectra of (D) fresh, gasoline reacted, and regenerated Ni-Mo/YSZ catalyst.

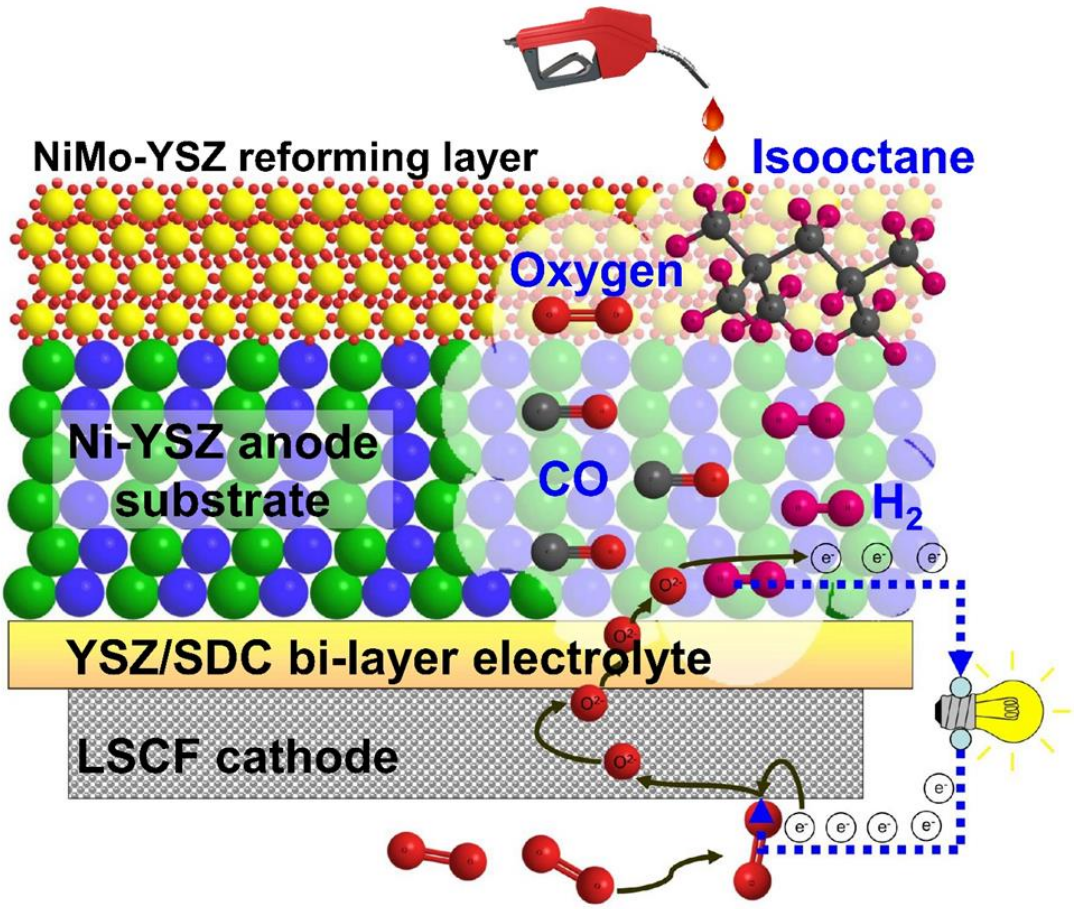

Figure 9. Schematic of button-typed SOFC with a micro-internal reforming layer under the direct isooctane/air feed condition at 750 °C.

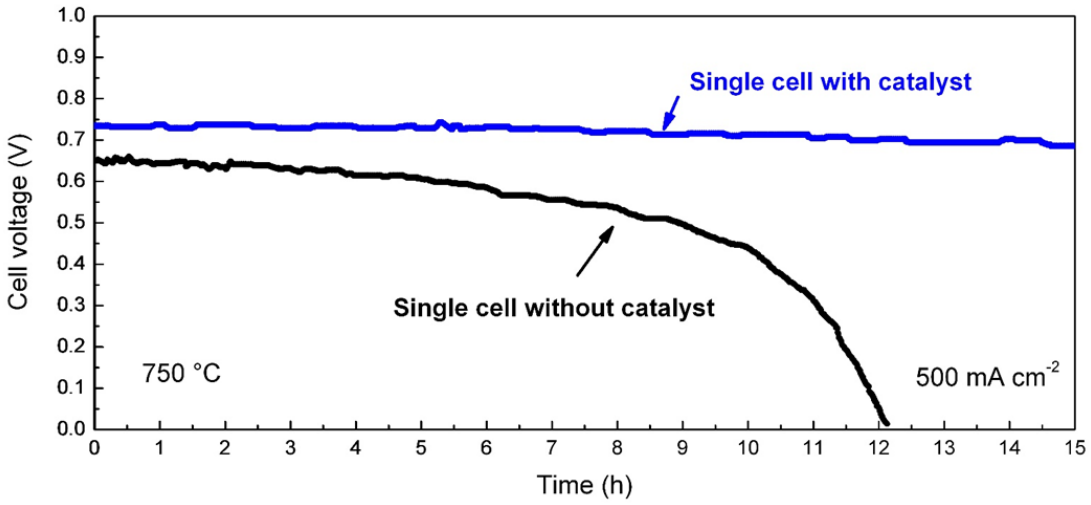

Figure 10. Performance stability of the Ni-YSZ anode-based SOFC with the Ni-Mo/YSZ catalyst layer at the constant current density of 500 mA cm^{-2}. During the 15 h performance stability test, the cell displays a low degradation rate of 0.003 V h^{-1} while the cell with no reforming layer died in 12 h.

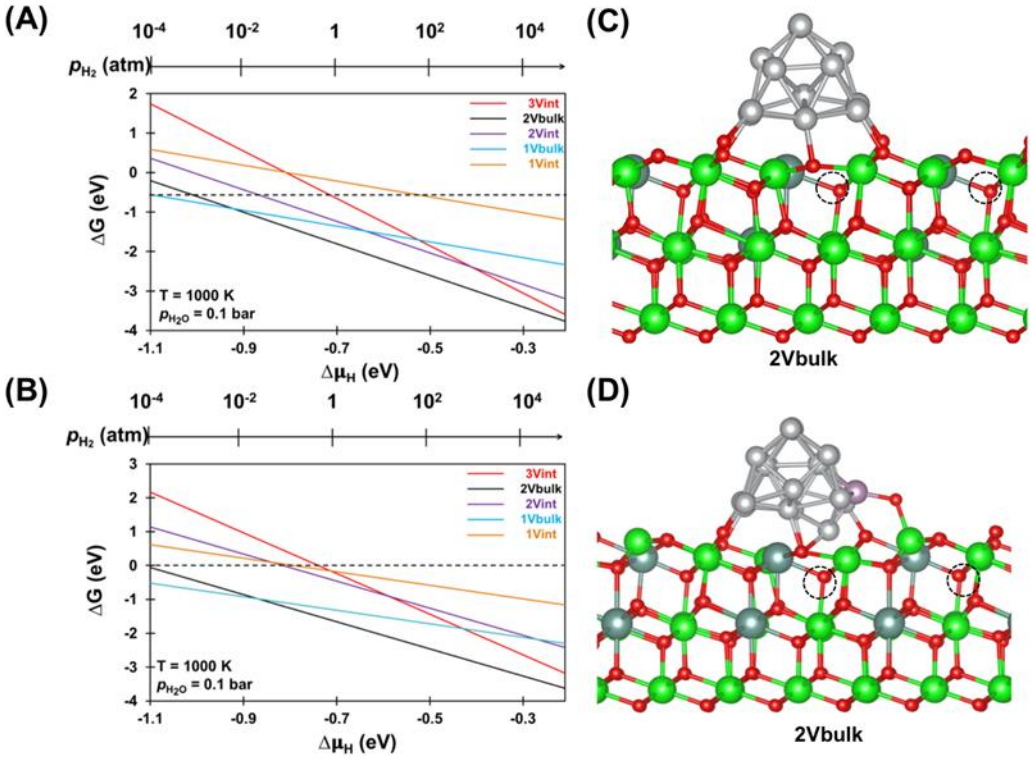

Figure 11. First principles-based phase diagram representing the relative equilibrium stabilities of the Ni/YSZ (A) and the Ni-Mo/YSZ (B) systems with various numbers of oxygen vacancies (the black dotted circles) as a function of the hydrogen chemical potential. Based on the phase diagram, the configurations shown in (C) and (D) are the most stable structure for the Ni/YSZ and the Ni-Mo/YSZ systems, respectively. The purple, silver, red, light green and dark green spheres represent Mo, Ni, O, Zr, and Y atoms, respectively. The nomenclature and the corresponding configurations for 3Vint, 2Vbulk, 2Vint, 1Vbulk and 1Vint models are given in the Supporting Information.

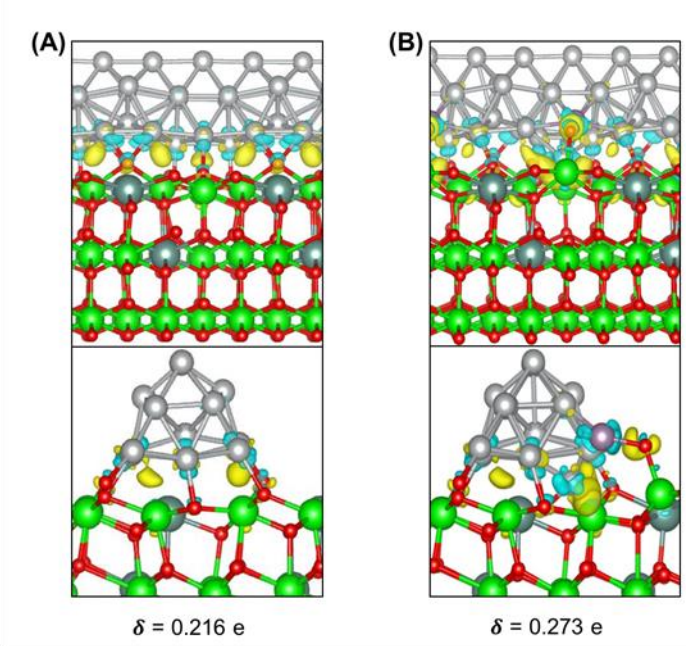

Figure 12. Differential charge densities showing that the electronic interaction between Ni-Mo clusters with the YSZ slab in the Ni-Mo/YSZ system (as shown in panel (B)) is stronger than that of Ni cluster in the Ni/YSZ system (as shown in panel (A)). The isosurface level of the differential charge densities are 0.01 e/Bohr^3. The yellow or blue areas represent a gain or loss of electrons.

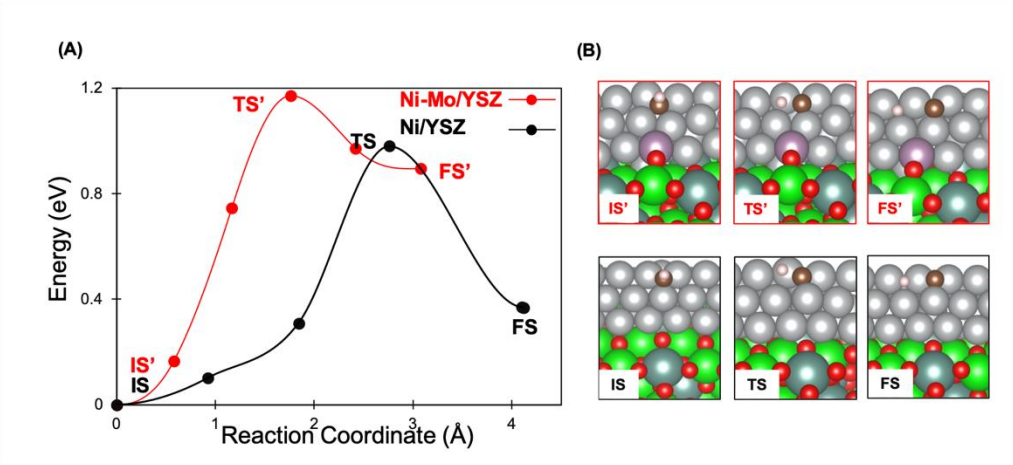

Figure 13. Transition state calculations for the C-H bond cleavage pathway over a Ni-Mo/YSZ and a Ni/YSZ catalyst (A) and their corresponding initial state (IS), transition state (TS), and final state (FS) configurations are depicted in panel (B). In the presence of Mo, the atomic positions of Ni-Mo/YSZ slab are fixed to assist the convergence of CINEB calculations of C-H dissociation.

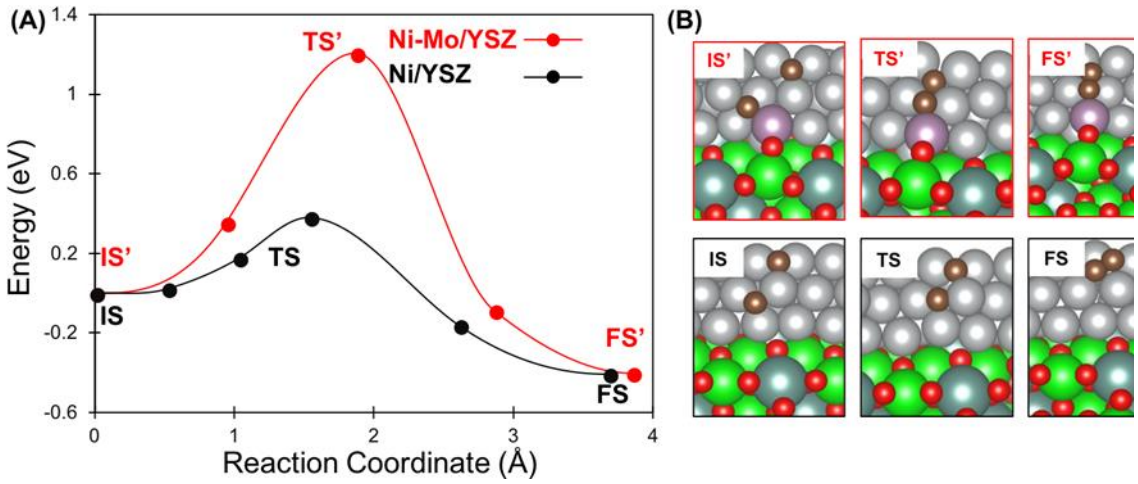

Figure 14. Transition state calculation for the C-C coupling pathway over a Ni-Mo/YSZ and a Ni/YSZ model system (A) and their corresponding initial state (IS), transition state (TS), and final state (FS) configurations are represented in part (B).

Enhancing the partial oxidation of gasoline with Mo-doped Ni catalysts for SOFC applications: An integrated experimental and DFT study

Qusay Bkour[a,‡], Fanglin Che[b,‡], Kyung-Min Lee[c], Chen Zhou[d], Nusnin Akter[c,d], Jorge Anibal Boscoboinik[d], Kai Zhao[e], Jake Gray[a], Steven R. Saunders[a,f], M. Grant Norton[a,g], J.-S. McEwen[a,f,h,i,j], Taejin Kim[c]*, Su Ha[a*]

[a]Voiland School of Chemical Engineering and Bioengineering, Washington State University, Pullman, WA 99164-2710, USA

[b]Department of Chemical Engineering, University of Massachusetts Lowell, Lowell, MA, 01854, USA

[c]Department of Materials Science and Chemical Engineering, Stony Brook University, Stony Brook, NY 11794, USA

[d]Center for Functional Nanomaterials, Brookhaven National Laboratory, Upton, NY 11973, USA

[e]School of Materials Science and Energy Engineering, Foshan University, Foshan 528000, China

[f]Department of Chemistry, Washington State University, Pullman, Washington 99164, United States

[g]School of Mechanical and Materials Engineering, Washington State University, P.O. Box 642920, Pullman, WA 99164-2920, USA

[h]Institute for Integrated Catalysis, Pacific Northwest National Laboratory, Richland, Washington 99352, United States

[i]Department of Physics and Astronomy, Washington State University, Pullman, Washington 99164, United States

[j]Department of Biological Systems Engineering, Washington State University, Pullman, Washington 99164, United States

1. Experimental Results

1.1 Effect of Mo on the Catalytic Performance

Table SI 1. Average crystallite sizes of Ni particles for fresh and isooctane POX spent catalyst samples. The addition of Mo to Ni/YSZ helps to maintain the small crystalline size of the Ni particles, maintaining Ni ensemble size below the point where coke formation becomes favorable.

Catalysts	Fresh [nm]	Spent [nm]
Ni/YSZ	16.1	26.1
NiMo/YSZ	8.2	10.3

Table SI 2. Summary of catalytic activity of different catalysts for POX of isooctane/gasoline.

Catalyst	Fuel content (mol%)	Feed ratio	T (°C)	TOS (h)	H_2 Yield	Conversion	Ref
Ni(5wt%)-Sn(0.5)/CZ	1 mol%	O_2/C=0.5	700	12	NA	73	[1]
MoO_2	1.6 mol%	O_2/C=0.7	700	7	94	100	[2]
Ni/Al_2O_3	2 mol%	O_2/C=0.5	600	30	30	48	[3]
Rh/Al_2O_3	2 mol%	O_2/C=0.5	600	30	44	57	[3]
Ni(11wt%)-Mo(3wt%)/YSZ	5 mol%	O_2/C=0.5	750	24	73	97	This work
Ni(11wt%)/YSZ	5 mol%	O_2/C=0.5	750	24	21	45	This work

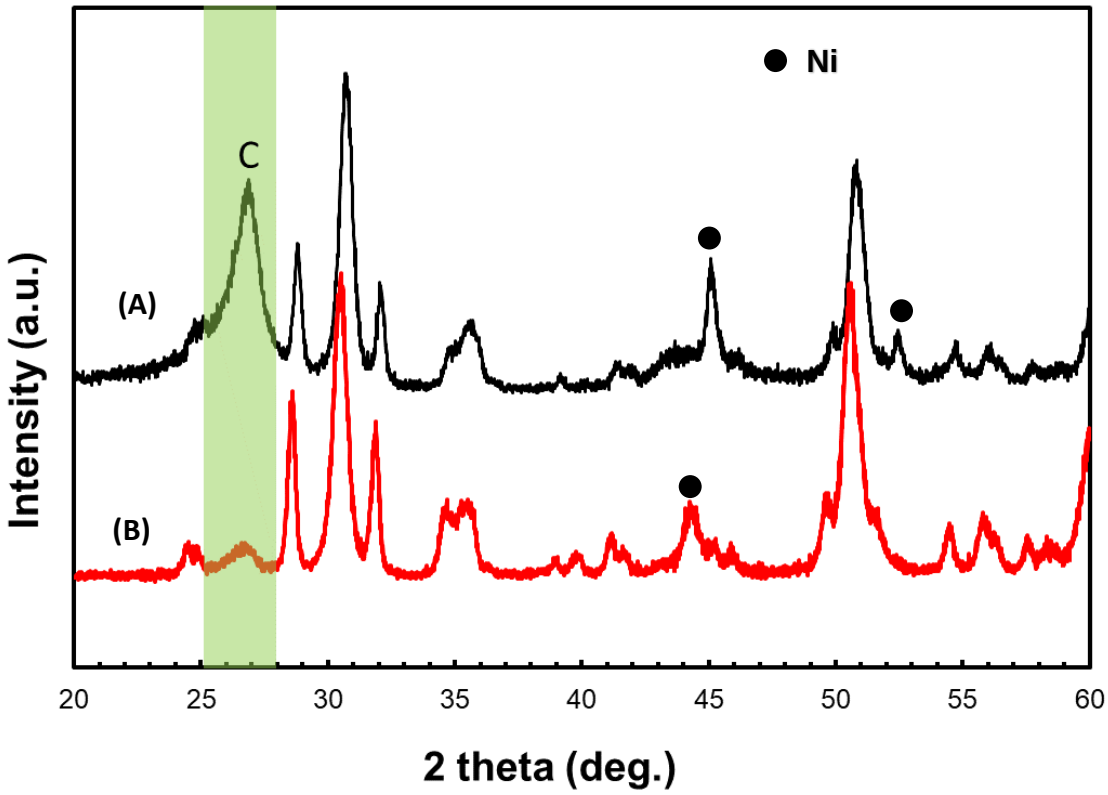

Figure SI 1. XRD patterns of (A) Ni/YSZ and (B) Ni-Mo/YSZ after 12 h of time-on-stream test for POX of gasoline. Spent samples show a much more intense peak of the carbon deposition for the Ni/YSZ sample compared to that of the Ni-Mo/YSZ sample.

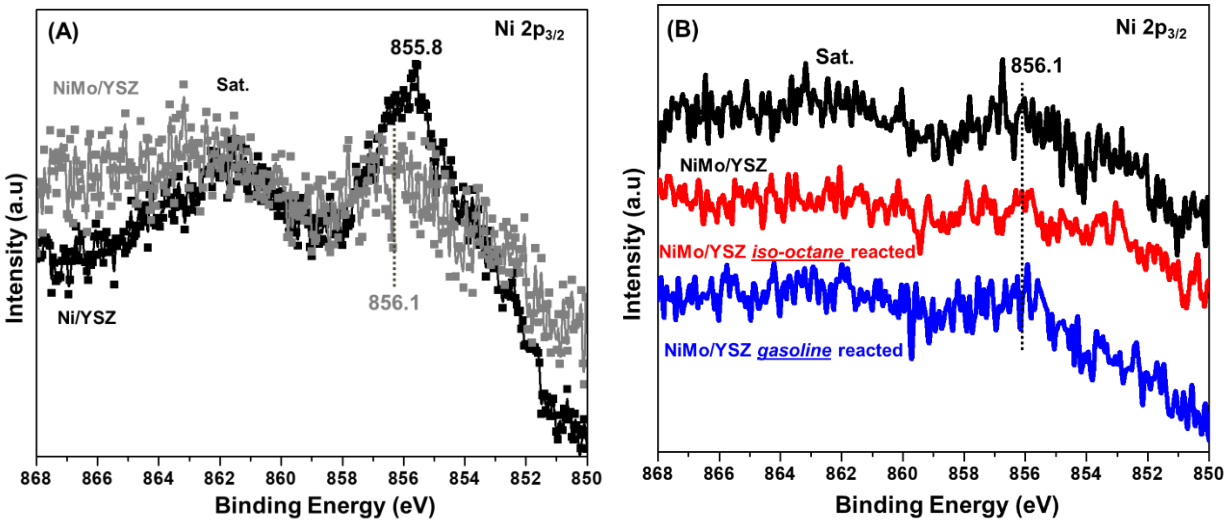

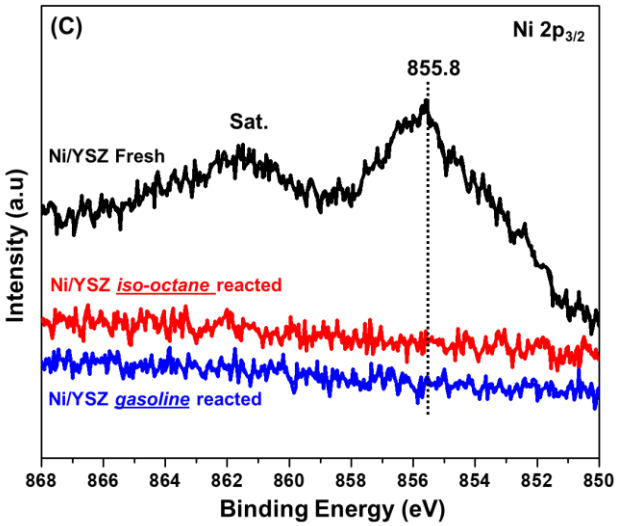

Figure SI 2. X-Ray photo-electron spectroscopy (XPS) spectra of (A) Ni 2*p*3/2 core level BE of fresh Ni/YSZ and Ni-Mo/YSZ, (B) Ni 2p3/2 core level BE of fresh and spent (iso-octane and gasoline) Ni-Mo/YSZ and (C) Ni 2p3/2 core level BE of fresh and spent (iso-octane and gasoline) Ni/YSZ.

Table SI 3. Average crystallite sizes for fresh and gasoline POX spent catalyst

Catalyst	Fresh [nm]	Spent [nm]
Ni/YSZ	16.1	26.8
Ni-Mo/YSZ	8.2	10.8

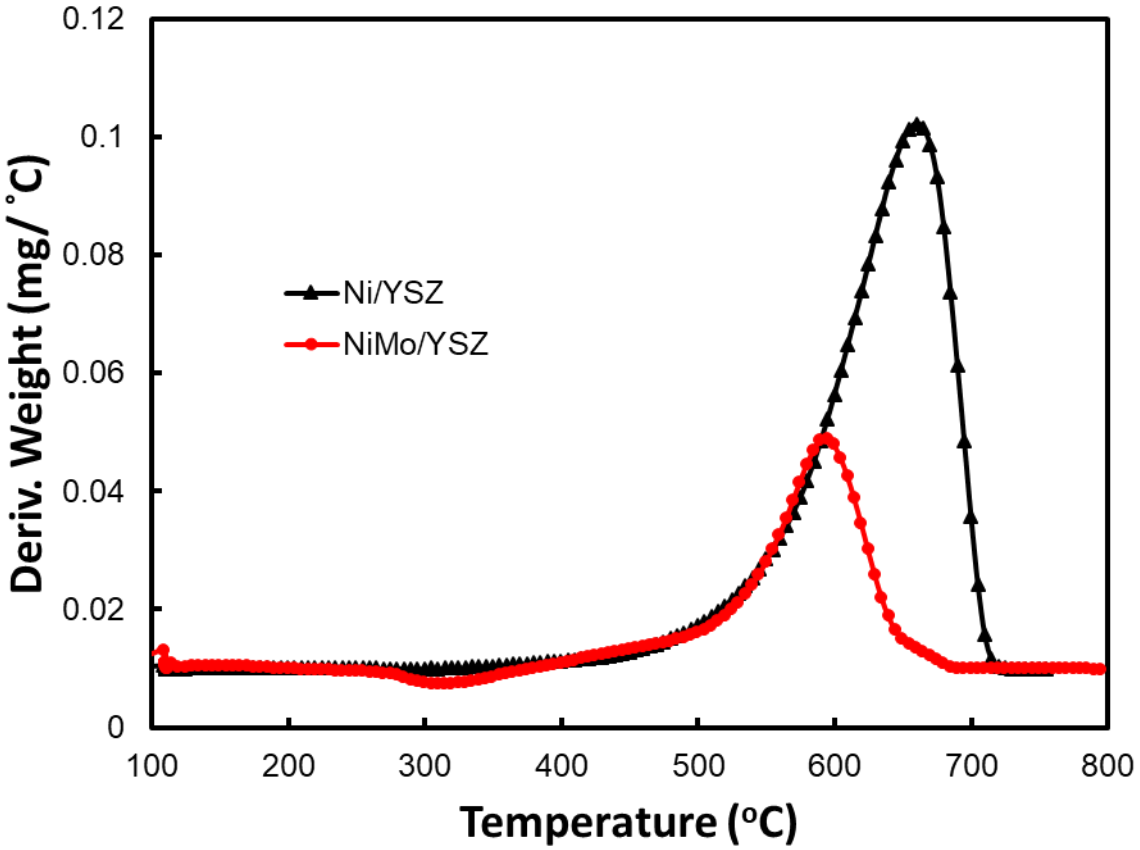

Figure SI 3. TGA derivatives curves of the weight loss as a function of temperature for Ni-Mo/YSZ and Ni/YSZ after 12 h of gasoline POX test (750 °C, WHSV of 13.8 h^{-1}, and O_2/C of 0.5). The derivative peak for the spent Ni/YSZ catalyst is shifted to higher temperature (660 °C) as compared to that of Ni-Mo/YSZ catalyst due to the higher degree of graphitization of the coke deposit.

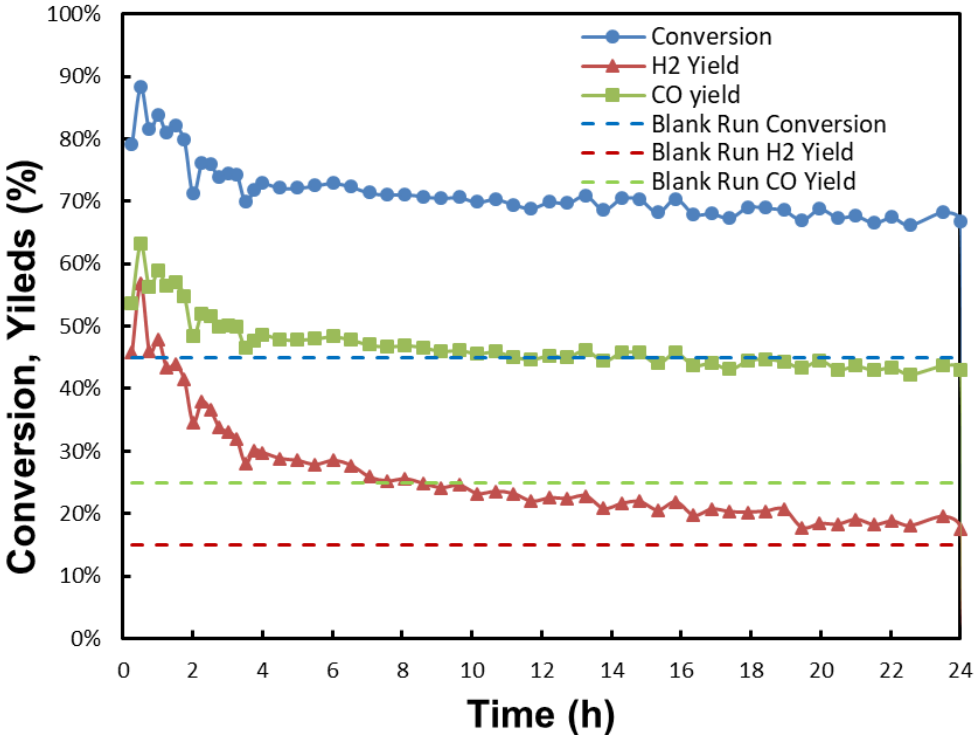

Figure SI 4. Catalytic activity of Ni-Sn/YSZ for the POX of isooctane at 750 °C, a O_2/C of 0.5 and a WHSV of 13.8 h^{-1}.

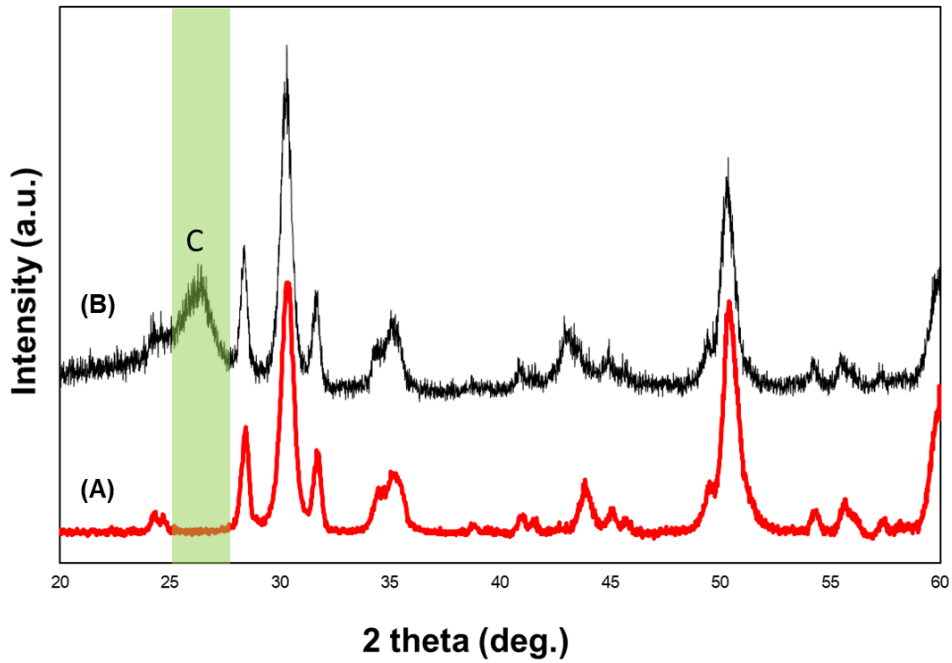

Figure SI 5. XRD patterns of fresh (A) and spent (B) Ni-Sn/YSZ samples. XRD analysis of the spent Ni-Sn catalyst indicates the formation of carbon deposits after 24 h operation.

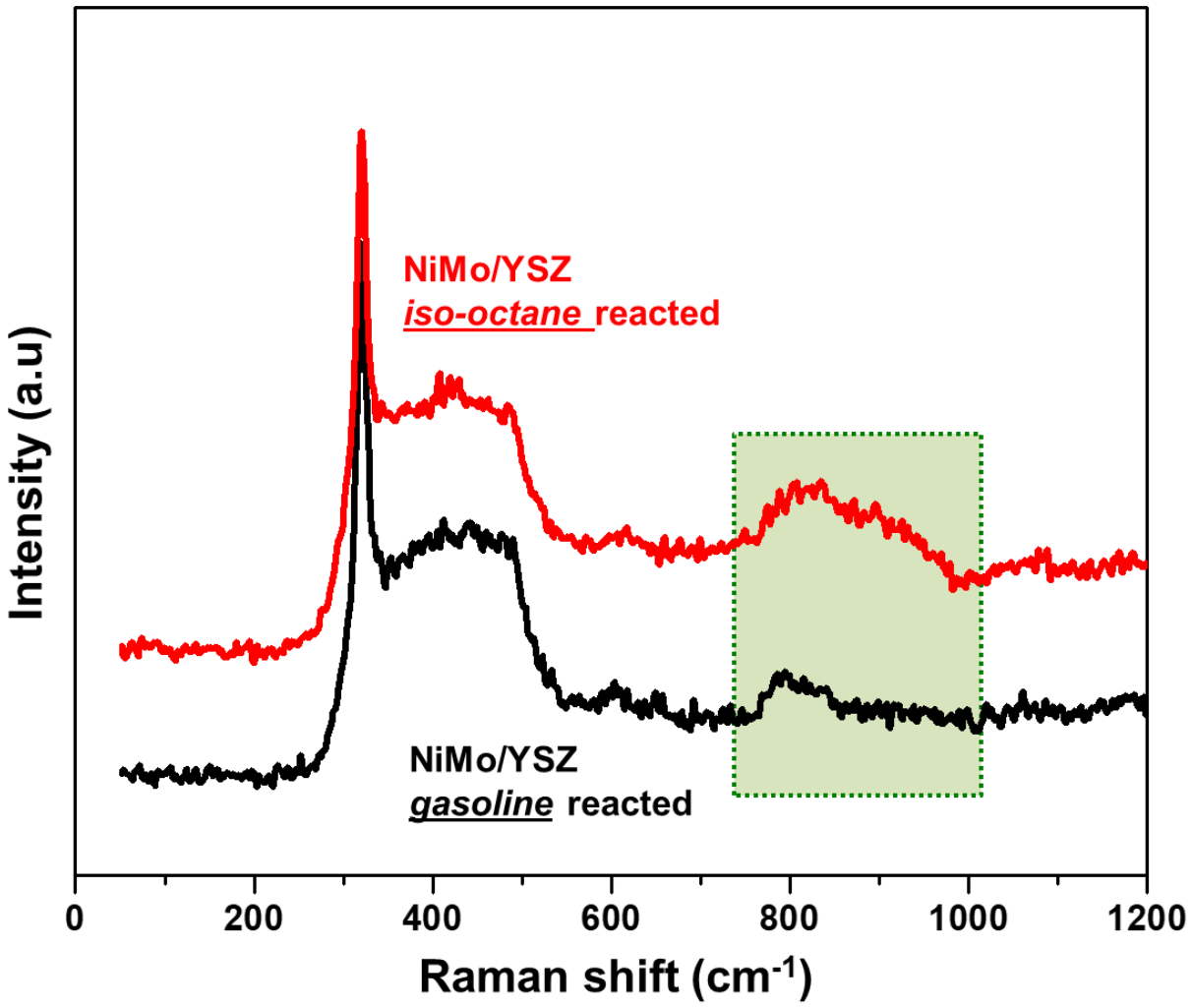

Figure SI 6. UV-Raman spectra of isooctane and gasoline reacted Ni/YSZ and Ni-Mo/YSZ catalysts.

1.2 Electrochemical Performance of Ni-Mo/YSZ as Internal Reforming Anode SOFC

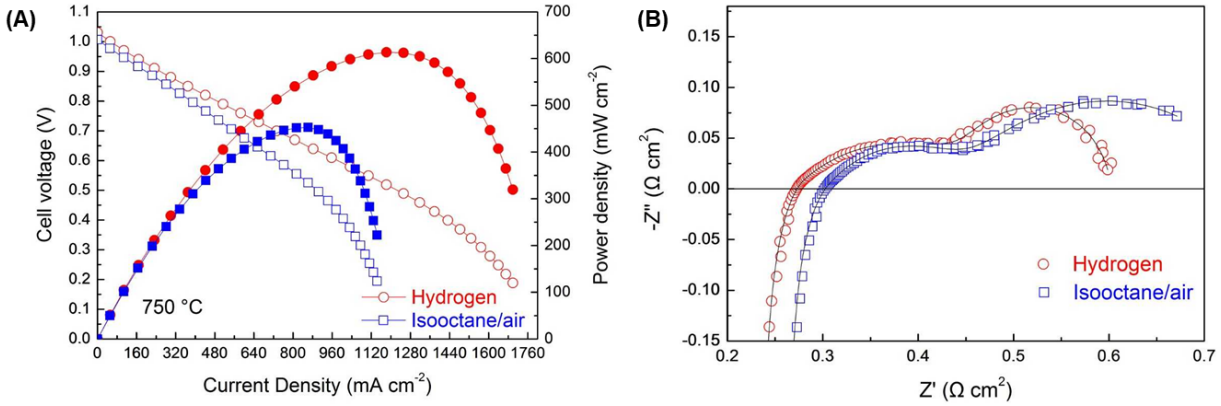

Figure SI 7. Electrochemical performance of the Ni-YSZ anode-based SOFC with the Ni-Mo/YSZ catalyst layer under hydrogen and isooctane/air operation modes at 750 °C: (A) Cell voltage and power density curves and (B) the Nyquist plots under the OCV condition.

Table SI 4. Electrochemical parameters of the button cell with the micro-reforming layer at 750 °C

Fuel	R_{ohm} (Ω cm^2)	R_H (Ω cm^2)	R_L (Ω cm^2)	R_P (Ω cm^2)	MPD (mW cm^{-2})
Hydrogen	0.23	0.24	0.13	0.37	613
Isooctane/air	0.25	0.21	0.29	0.50	452

2. Computational Details

2.1 Nomenclature

To obtain the first principles-based phase diagram in the main manuscript, we examines the relative equilibrium stability of the Ni/YSZ cermet (or Ni-Mo/YSZ cermet) with various oxygen vacancy concentrations under relevant experimental conditions. In this section, we clarify our nomenclature.

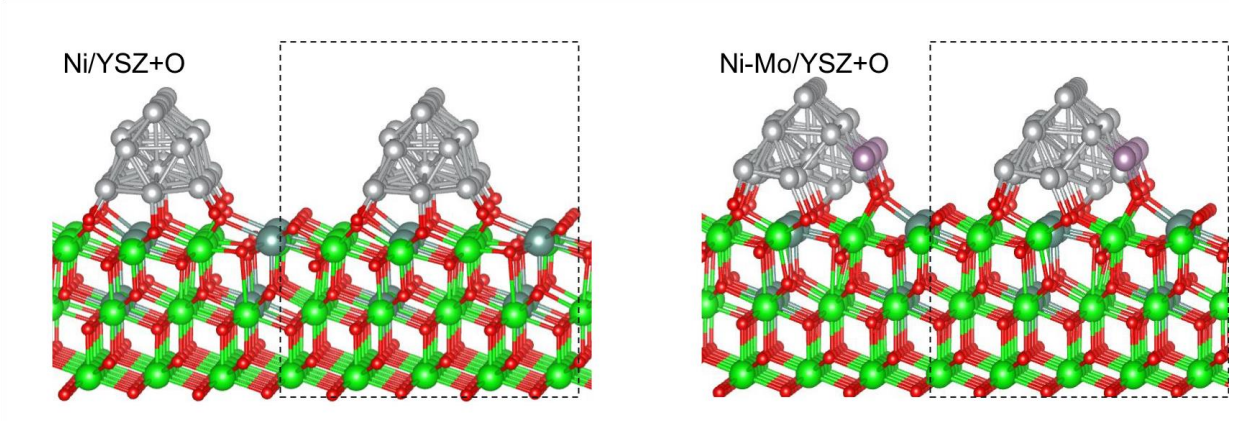

Figure SI. 8. The optimized configurations for the Ni/YSZ+O and the Ni-Mo/YSZ+O systems. The purple, silver, red, light green and dark green spheres represent Mo, Ni, O, Zr, and Y atoms, respectively.

'Ni/YSZ+O' (or Ni-Mo/YSZ+O cermet), as shown in Figure SI 8, represents the oxygen-enriched Ni/YSZ cermet (or Ni-Mo/YSZ cermet) with a 18-atom Ni cluster supported by 2 Y_2O_4 and 20 ZrO_2 formula units. After taking the most favorable interface oxygen atom, it forms the Ni/YSZ+½O model or Ni-Mo/YSZ+½O model (here '1/2' stands for ½ extra O atom per stoichiometric YSZ unit), which has only one interface oxygen vacancy (1Vint.). When we remove a subsurface oxygen anion with the lowest oxygen vacancy formation energy from the 'Ni/YSZ+O' cermet (or Ni-Mo/YSZ+O cermet), it forms the Ni/YSZ+½O (or Ni-Mo/YSZ+½O) model with only one subsurface vacancy (1Vbulk.). In addition, after removing two subsurface oxygen atoms with the lowest oxygen vacancy formation energies from the Ni/YSZ+O (or Ni-Mo/YSZ+O) cermet one forms the Ni/YSZ (or Ni-Mo/YSZ) model with two subsurface oxygen vacancies (2Vbulk.). The '2Vint.' model represents the Ni/YSZ+O (or Ni-Mo/YSZ+O) model and includes one interface oxygen vacancy (1Vint.) and one subsurface oxygen vacancy (1Vbulk.). The '3Vint.' model includes two subsurface oxygen vacancies (2Vbulk) and one interface oxygen vacancy

(1Vint.) inside the Ni/YSZ+O model. The configurations for the Ni-Mo/YSZ model with various oxygen vacancy concentrations are presented in Figure SI 9. We also examined different adsorption sites for Mo atoms for the Ni-Mo/YSZ model, as shown in Figure SI10. Among all the Ni-Mo/YSZ configurations, the Ni-Mo/YSZ_2 and Ni-Mo/YSZ_4 are the most favorable structures. Based on the previous publication (4), the interface oxygen vacancy is easier to form on the right side of the Ni cluster in the Ni/YSZ system, which will lead to the formation of coke. The presence of Mo on the left side of the Ni cluster will not affect the catalytic reactivity of the interfacial sites on the right side of the Ni cluster. Thus, we considered the Ni-Mo/YSZ_2 configuration as our structure to study the effects of Mo dopants on the formation of coke. In addition, when Mo sits over the right side of the Ni cluster in Ni-Mo/YSZ, the smallest binding energy difference for Mo between the most favorable interfacial site (between the Ni cluster and YSZ support) and when it only binds to the Ni cluster is 0.72 eV. This makes sense because the Mo adspecies form a covalent bond with the O species at interface site between Ni cluster and YSZ support, which is much stronger than the metallic bond between the Ni cluster and the Mo adspecies. Further, we note that it is not energetically favorable to incorporate Mo inside the Ni cluster because of its large size. The oxygen vacancy formation energies in Ni/YSZ+O and Ni-Mo/YSZ+O are given in Table SI 5. More details regarding the computational setup for the Ni/YSZ system can be found in our previous works (5-7).

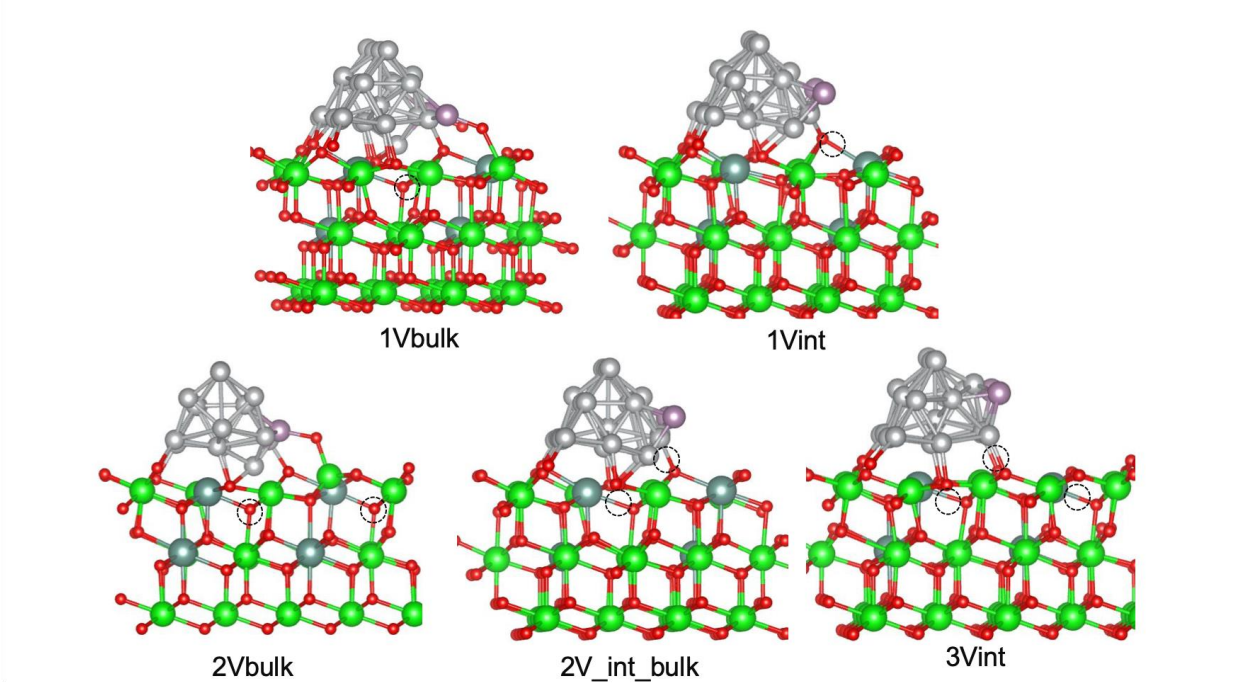

Figure SI 9. The configurations for the Ni-Mo/YSZ model with various oxygen vacancy concentrations, as presented in the phase diagram in the main manuscript. The sphere legend is as in Figure SI 8.

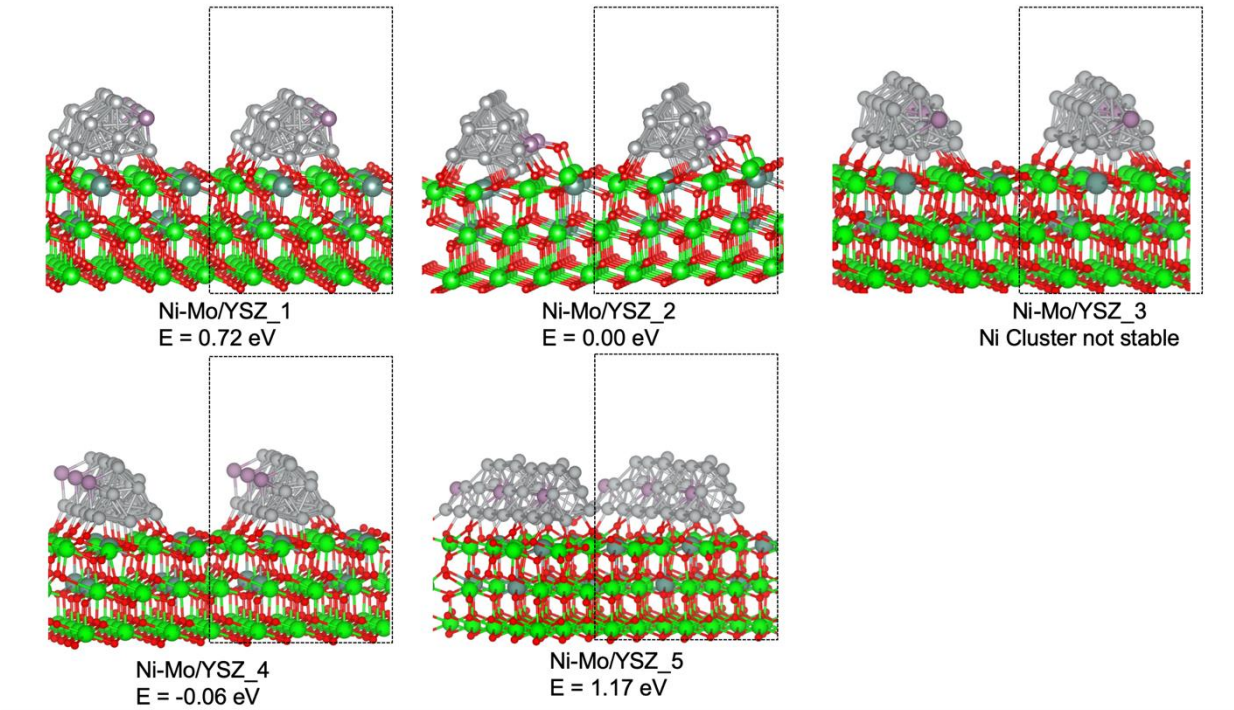

Figure SI 10. The optimized configurations for the Ni-Mo/YSZ system with different Mo adsorption sites. Mo binds more favorably at the interface between the Ni cluster and the YSZ support (conformation Ni-Mo/YSZ_2) or on the left-hand side of the Ni cluster (conformation Ni-Mo/YSZ_4). The energy (E) of the Ni-Mo/YSZ conformations are referenced with respect to Ni-Mo/YSZ_2 conformation. We note that the Ni-Mo/YSZ_5 conformation was rotated by 180° in order to be able to see where the Mo site is incorporated in the Ni cluster. The conformation with a positive energy value denotes the unstable structures. The sphere legend is as in Figure SI 8.

Table SI 5. The oxygen vacancy formation energies in the Ni/YSZ+O and Ni-Mo/YSZ+O models.

	Vacancy type	E_f (eV)
Ni/YSZ	3Vint	1.85
	2Vint	0.44
	2Vbulk	-0.13
	1Vint	0.62
	1Vbulk	-0.52
Ni-Mo/YSZ	3Vint	2.28
	2Vint	1.21
	2Vbulk	0.01
	1Vint	0.65
	1Vbulk	-0.49

2.2 First Principles-based Phase Diagram

The Gibbs free energy change of adsorption (ΔG) as a function of the hydrogen chemical potential ($\Delta\mu_H$) can provide us with a connection between our DFT calculations and the relative equilibrium stabilities of the Ni/YSZ+O ($Ni_{18}Y_2Zr_{22}O_{48}$) or the Ni-Mo/YSZ+O ($Ni_{18}Mo_1Y_2Zr_{22}O_{48}$) system with various oxygen vacancy concentrations under various experimental conditions (8-11). The following paragraph explains how we define ΔG based on our calculations.

The oxygen vacancy formation in Ni/YSZ+O (or Ni-Mo/YSZ+O) via the hydrogen reduction reaction is shown in Eq. (1) and the oxygen vacancy formation energy E_f (1Vint., 1Vbulk., 2Vbulk., 3Vint.) is defined in Eq. (2).

$$\mathrm{Ni_{18}Y_2Zr_{22}O_{48}} + \mathrm{xH_2} \leftrightarrow \mathrm{Ni_{18}Y_2Zr_{22}O_{48-x}} + \mathrm{xH_2O} \quad (1)$$

$$E_f(\mathrm{Ni_{18}Y_2Zr_{22}O_{48-x}}) = E(\mathrm{Ni_{18}Y_2Zr_{22}O_{48-x}}) + \mathrm{xE_{H_2O}} - E(\mathrm{Ni_{18}Y_2Zr_{22}O_{48}}) - \mathrm{xE_{H_2}} \quad (2)$$

Where $E(\mathrm{Ni_{18}Y_2Zr_{22}O_{48-x}})$ is the total energy of the Ni/YSZ+O (Ni-Mo/YSZ+O) systems with various oxygen vacancies. $E(\mathrm{Ni_{18}Y_2Zr_{22}O_{48}})$ is the total energy of the Ni/YSZ+O (Ni-Mo/YSZ+O) with no oxygen vacancies. $E_{\mathrm{H_2O}}$ and $E_{\mathrm{H_2}}$ represent the gas phase energies of H_2O and H_2, respectively. ΔG is then obtained by Eq. (3).

$$\Delta G = E_f(\mathrm{Ni_{18}Y_2Zr_{22}O_{48-x}}) + x\Delta\mu_{\mathrm{H_2O}} - 2x\Delta\mu_{\mathrm{H}} \quad (3)$$

Where $\Delta\mu_H$ is defined as $\Delta\mu_H = \mu_H - \frac{1}{2}E_{H_2}$, since we take H_2 as the hydrogen reference. Similarly, we can also get $\Delta\mu_{\mathrm{H_2O}}$ defined as $\Delta\mu_{\mathrm{H_2O}} = \mu_{\mathrm{H_2O}} - E_{\mathrm{H_2O}}$. At 0 K and standard pressure conditions, we define $\mu_H\left(0\ \mathrm{K}, p_0^{\mathrm{H_2}}\right) = \frac{1}{2}E_{\mathrm{H_2}} \equiv 0$ and $\mu_{\mathrm{H_2O}}\left(0\ \mathrm{K}, p_0^{\mathrm{H_2O}}\right) = E_{\mathrm{H_2O}} \equiv 0$.

From above paragraphs, we have completely described how we obtain ΔG from our DFT calculations as a function of hydrogen chemical potential. We can also relate the $\Delta\mu_H$ to a realistic temperature and hydrogen partial pressure, as shown in Eq. (4) and (5). Here we assume that the $2\mathrm{H} \rightarrow \mathrm{H_2}$ reaction is in quasi-equilibrium.

$$\Delta\mu_{\mathrm{H}}(T,\ p^{\mathrm{H_2}}) = \Delta\mu_{\mathrm{H}}\left(T, p_0^{\mathrm{H_2}}\right) + \frac{1}{2}k_{\mathrm{B}}Tln\frac{p}{p_0} \quad (4)$$

$$\Delta\mu_{\mathrm{H}}\left(T, p_0^{\mathrm{H_2}}\right) = \frac{1}{2}\left[H\left(T, p_0^{\mathrm{H_2}}\right) - H\left(0\ \mathrm{K}, p_0^{\mathrm{H_2}}\right)\right] - \frac{1}{2}T\left[S\left(T, p_0^{\mathrm{H_2}}\right) - S\left(0\ \mathrm{K}, p_0^{\mathrm{H_2}}\right)\right] \quad (5)$$

Where p^{H_2} and $p_0^{H_2}$ represent the practical partial pressure and standard partial pressure (1 atm) of H_2, and k_B is Boltzmann's constant. Eq. (4) provides us with a description of how the hydrogen chemical potential is altered by the pressure at a given temperature. Additionally, with respect to $\Delta\mu_H(0\ K,\ p^{H_2})$, $\Delta\mu_H\left(T, p_0^{H_2}\right)$ is given in Eq. (5). The values of the enthalpy H and the entropy S at a given temperature and standard pressure can be found in Thermodynamic Tables[10]. Similar to $\Delta\mu_H(T,\ p^{H_2})$, we can calculate $\Delta\mu_{H_2O}(T,\ p^{H_2O})$ as well.

3. Theoretical Results

3.1 C-H adsorption

Since C in CH has three unpaired electrons, it is more stable to adsorb at the hollow sites (fcc and hcp) of Ni cluster as compared to the top and bridge sites. This has been confirmed by our previous publication (12) Thus, in this work, only hollow sites of the Ni cluster in the Ni/YSZ or Ni-Mo/YSZ model for CH species were examined.

Zhang et al. (13) has shown that when CH adsorbs between the 1st and 2nd top layer of Ni cluster in Ni/YSZ, the adsorption energies of CH at the hollow sites (fcc and hcp) are nearly the same, ~ -6.30 eV. Our results further confirm this, as shown in the top picture of Figure S11(A). Zhang et al. (13) also showed that when CH adsorbs at the hollow sites between the 2nd and 3rd layer of Ni cluster in Ni/YSZ and the adsorption site is far from the oxygen vacancy at the interface, the adsorption energies of CH at fcc and hcp sites are nearly the same. Since we don't have an oxygen vacancy at the interface, we only examined one CH configuration at the hollow site between the 2nd and the 3rd

layer of the Ni cluster in our Ni/YSZ model. The adsorption energy of CH is -5.84 eV, as shown in the bottom picture of Figure S11(A). Similarly, we also examined these sites of CH over Ni-Mo/YSZ, as presented in Figure S11(B).

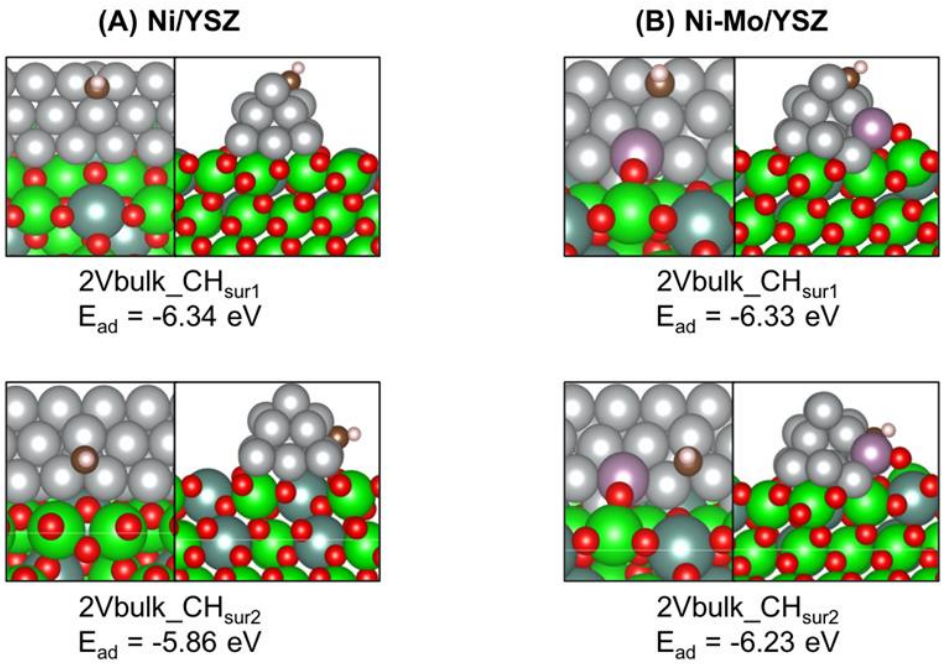

Figure SI. 11. The optimized configurations for the adsorption of CH adspecies over Ni/YSZ and Ni-Mo/YSZ (2Vbulk). The sphere legend is same as in Figure SI 8.

The adsorption energies (E_{ad}) in Figure SI 11 for the CH group over the Ni/YSZ and the Ni-Mo/YSZ models were calculated using Eq.(S1)

$$E_{\mathrm{ad}} = E_{\mathrm{CH/slab}} - E_{\mathrm{slab}} - E_{\mathrm{CH}} \quad \text{(S1)}$$

Where $E_{\mathrm{CH/slab}}$, E_{slab}, and E_{CH} denote for the calculated energies of CH species over Ni/YSZ (or Ni-Mo/YSZ), the Ni/YSZ (or Ni-Mo/YSZ) slab, and the CH radical in a box, respectively. Our calculated CH adsorption energy of ~-6.34 eV is similar to the CH adsorption energy of ~-6.30 eV in other benchmarking literature (13).

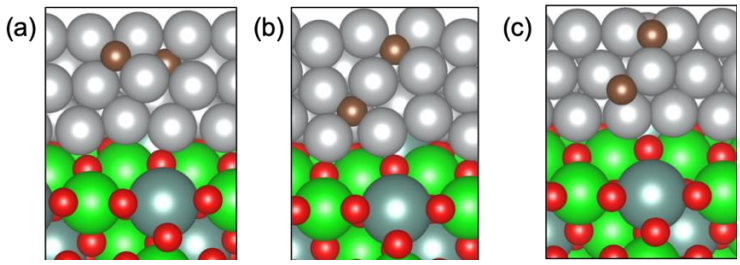

Figure SI. 12. The adsorption configurations that were tested for the coadsorption of two carbon atoms over a Ni/YSZ catalyst. Only configuration (c) is stable and didn't alter the Ni/YSZ structure. The sphere legend is as in Figure SI 8.

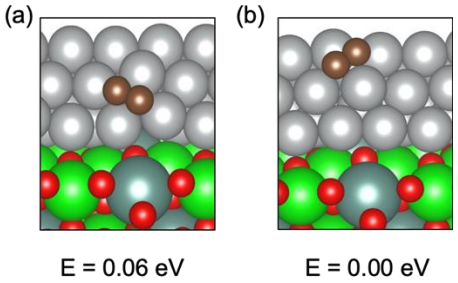

Figure SI. 13. The adsorption configurations that were tested for the adsorption of a C=C species over a Ni/YSZ catalyst. Configuration (b) is 0.06 eV more stable than configuration (a). The sphere legend is as in Figure SI 8.

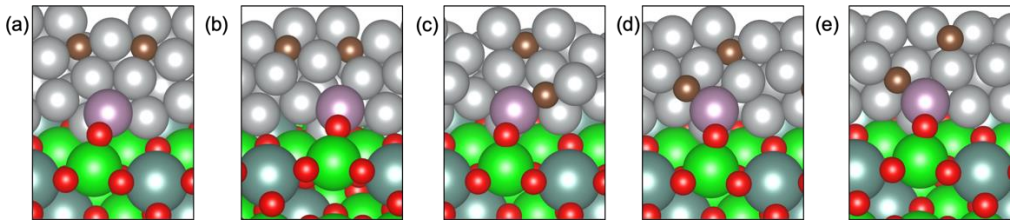

Figure SI. 14. The adsorption configurations that were tested for the coadsrption of two carbon atoms over a Ni-Mo/YSZ catalyst. Only configuration (e) is stable and didn't alter the Ni-Mo/YSZ structure. The sphere legend is as in Figure SI 8.

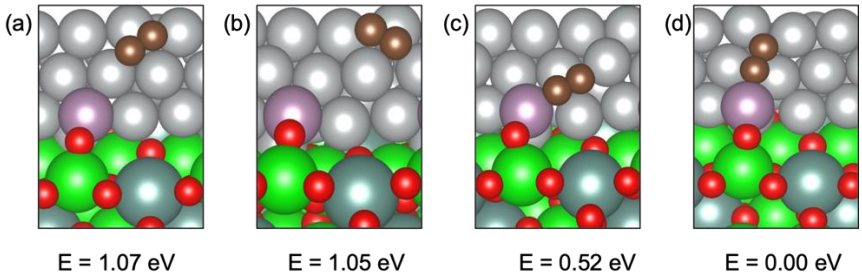

Figure SI. 15. The adsorption configurations that were tested for the adsorption of a C=C species over a Ni-Mo/YSZ catalyst. Configuration (d) the most stable one as compared to configurations (a)-(c). The sphere legend is as in Figure SI 8.

3.2 C-H bond cleavage and C-C coupling reactions over flat surfaces

We also examined the C-H bond cleavage and C-C bond coupling reactions over Ni(111) and Ni-Mo(111) models, as shown in Figures SI 12 and SI 13. For Ni(111), a four-layer metal slab was modeled using a p(3×3) supercell (4) with the two bottom layers fixed at their equilibrium (i.e., bulk phase positions), while the upper layers were allowed to relax. The Ni lattice constant was theoretically calculated and was found to be 3.521 Å and is within 0.08% of the experimental value of 3.524 Å (14). The periodically repeating unit cells were separated by 11 Å of vacuum. This is comparable to the values used in the literature, which range from 10 Å to 12 Å (15) to ensure that adsorbates and the subsequent slab would have minimal interactions. A planewave basis set was expanded to a kinetic energy maximum of 400 eV for the Kohn–Sham orbitals. A first-order Methfessel–Paxton smearing method with width of 0.1 eV was used to account for partial occupancies around the Fermi level and to speed up the convergence. The Brillouin zone integration was approximated by a sum over k-points chosen using a Monkhorst–Pack mesh with a grid of (4 × 4 × 1) k-points. Geometries were considered optimized when the energy had converged to 10^{-4} eV and the forces were smaller than 0.03 eV $Å^{-1}$. In addition, all the calculations included spin-polarization. For the Ni-Mo(111) model, one of the Ni atom on the surface layer was replaced by Mo and other computational set up keeps the same as Ni(111). More details can be referred to our previously publication (16).

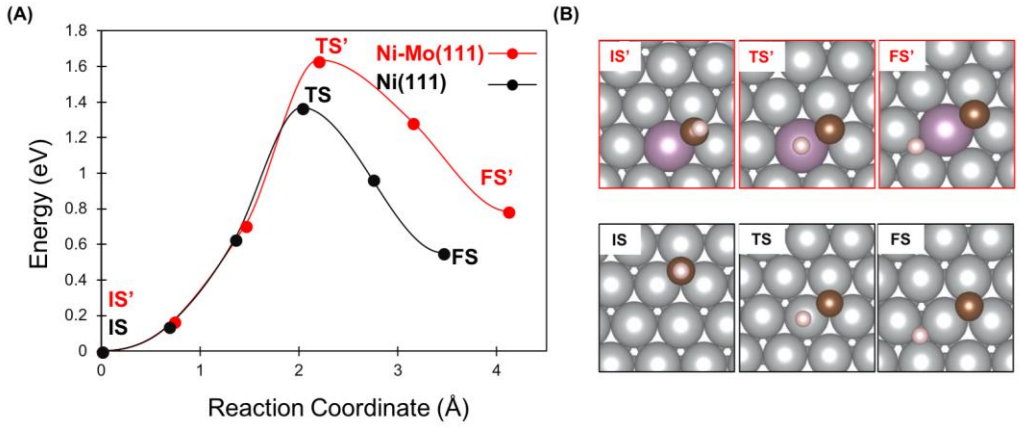

Figure SI. 16. Transition state calculations on C-H cleavage over Ni-Mo(111) and Ni(111) (A) and their corresponding initial state (IS), transition state (TS), and final state (FS) configurations are presented in part (B).

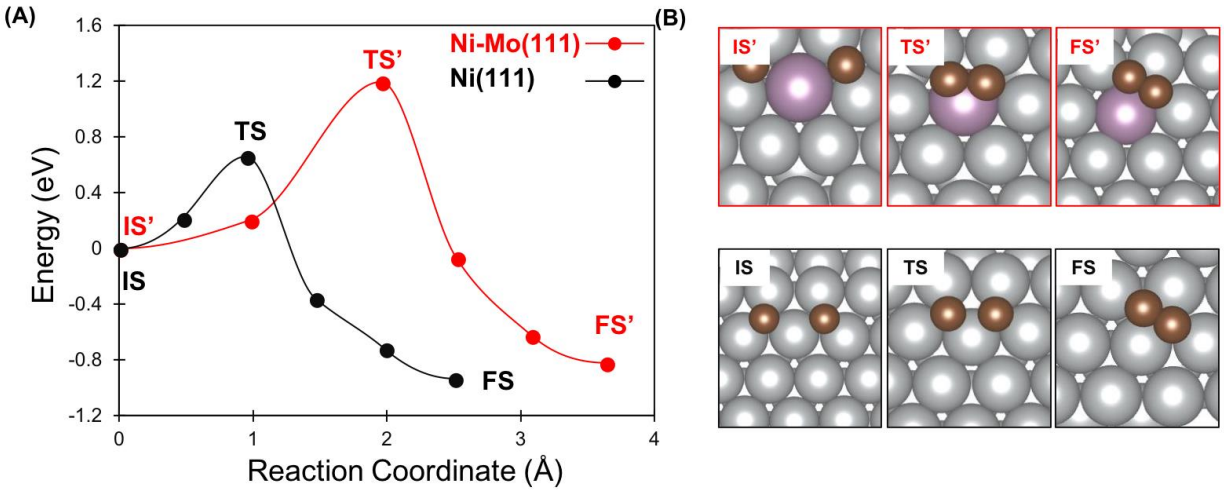

Figure SI. 17. Transition state calculations on C-C coupling over Ni-Mo(111) and Ni(111) (A) and their corresponding initial state (IS), transition state (TS), and final state (FS) configurations are presented in part (B).

3.3 Electronic properties of Ni(111) and NiMo(111)

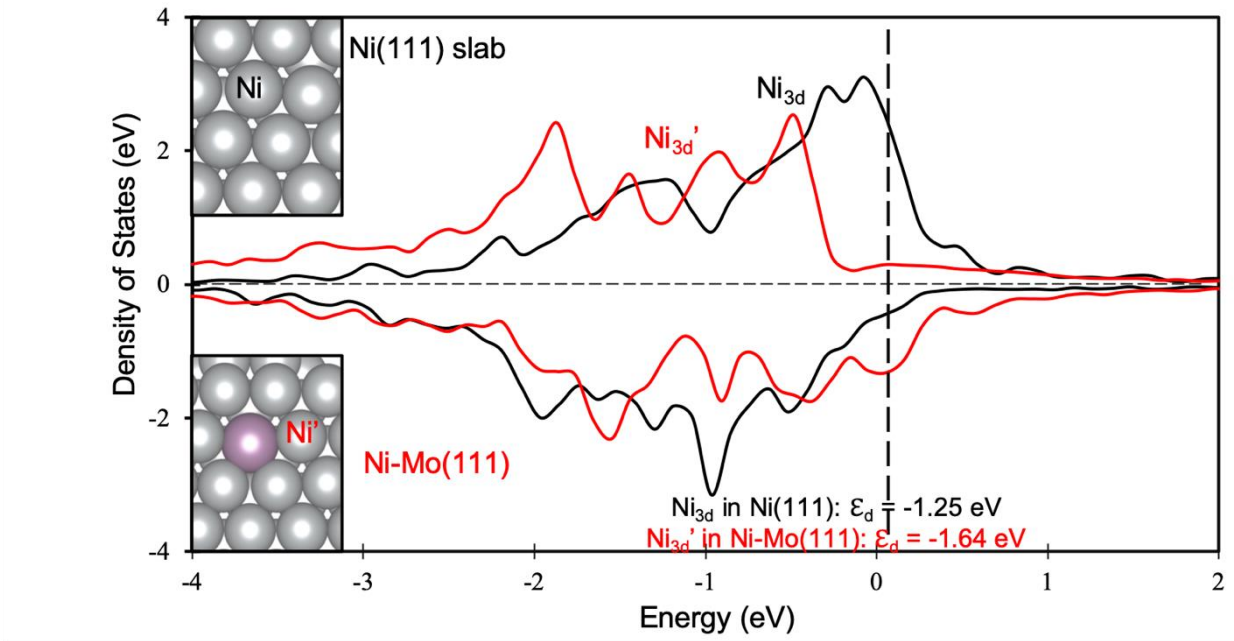

Figure SI. 18. The projected density of state (PDOS) of Ni3d orbital of the Ni atom in the Ni(111) and Ni-Mo(111) systems. The sphere legend is as in Figure SI 8.

References

(1) Pengpanich, S.; Meeyoo, V.; Rirksomboon, T.; Schwank, J. Iso-Octane Partial Oxidation over Ni-Sn/$Ce_{0.75}Zr_{0.25}O_2$ Catalysts. *Catal. Today* **2008**, *136* (3–4), 214–221. https://doi.org/10.1016/j.cattod.2008.01.018.

(2) Marin Flores, O. G.; Ha, S. Activity and Stability Studies of MoO_2 Catalyst for the Partial Oxidation of Gasoline. *Appl. Catal. A Gen.* **2009**, *352* (1–2), 124–132. https://doi.org/10.1016/j.apcata.2008.09.036.

(3) López-Fonseca R, Jiménez-González C, Gil-Calvo M, De Rivas B, Gutiérrez-Ortiz JI. Partial oxidation of Gasoline over Ni/Al_2O_3 catalysts using nickel aluminate as precursor. Chem Eng Trans. **2017**, 955-960.

(4) S.-G. Wang, D.-B. Cao, Y.-W. Li, J. Wang, H. Jiao, Chemisorption of CO2 on Nickel Surfaces, The Journal of Physical Chemistry B, 109 (**2005**) 18956-18963.

(5) Che, F.; Ha, S.; McEwen, J. S. Elucidating the Role of the Electric Field at the Ni/YSZ Electrode: A DFT Study. *J. Phys. Chem. C* **2016**, *120* (27), 14608–14620. https://doi.org/10.1021/acs.jpcc.6b01292.

(6) Che, F.; Ha, S.; McEwen, J. S. Catalytic Reaction Rates Controlled by Metal Oxidation State: C−H Bond Cleavage in Methane over Nickel-Based Catalysts. *Angew. Chemie - Int. Ed.* **2017**, *56* (13), 3557–3561. https://doi.org/10.1002/anie.201611796.

(7) Che, F.; Ha, S.; McEwen, J. S. Hydrogen Oxidation and Water Dissociation over an Oxygen-Enriched Ni/YSZ Electrode in the Presence of an Electric Field: A First-Principles-Based Microkinetic Model. *Ind. Eng. Chem. Res.* **2017**, *56* (5), 1201–1213. https://doi.org/10.1021/acs.iecr.6b04028.

(8) McEwen, J. S.; Anggara, T.; Schneider, W. F.; Kispersky, V. F.; Miller, J. T.; Delgass, W. N.; Ribeiro, F. H. Integrated Operando X-Ray Absorption and DFT Characterization of Cu-SSZ-13 Exchange Sites during the Selective Catalytic Reduction of NOx with NH_3. In *Catalysis Today*; **2012**; Vol. 184, pp 129–144. https://doi.org/10.1016/j.cattod.2011.11.037.

(9) Reuter, K.; Stampf, C.; Scheffler, M. AB Initio Atomistic Thermodynamics and Statistical Mechanics of Surface Properties and Functions. In *Handbook of Materials Modeling*; **2005**; pp 149–194. https://doi.org/10.1007/978-1-4020-3286-8_10.

(10) Getman, R. B.; Xu, Y.; Schneider, W. F. Thermodynamics of Environment-Dependent Oxygen Chemisorption on Pt(111). *J. Phys. Chem. C* **2008**, *112* (26), 9559–9572. https://doi.org/10.1021/jp800905a.

(11) Reuter, K.; Scheffler, M. Composition, Structure and Stability of RuO_2(110) as a Function of Oxygen Pressure. *Phys. Rev. B* **2001**, *65* (July), 035406. https://doi.org/10.1103/PhysRevB.65.035406.

(12) F. Che, R. Zhang, A.J. Hensley, S. Ha, J.-S. McEwen, Density functional theory studies of methyl dissociation on a Ni(111) surface in the presence of an external electric field, Phys. Chem. Chem. Phys, **2014**, 6, 2399-2410.

(13) Y. Zhang, Z. Fu, M. Wang, Z. Yang, Oxygen vacancy induced carbon deposition at the triple phase boundary of the nickel/yttrium-stabilized zirconia (YSZ) interface, J. Power Sources, **2014**, 261, 136-140.

(14) A.A. Phatak, W.N. Delgass, F.H. Ribeiro, W.F. Schneider, Density Functional Theory Comparison of Water Dissociation Steps on Cu, Au, Ni, Pd, and Pt, The Journal of Physical Chemistry C, **2009**, 113, 7269-7276.

(15) H. Liu, R. Yan, R. Zhang, B. Wang, K. Xie, A DFT theoretical study of CH4 dissociation on gold-alloyed Ni(111) surface, Journal of Natural Gas Chemistry, **2011**, 20, 611-617.

(16) F. Che, R. Zhang, A.J. Hensley, S. Ha, J.-S. McEwen, Density functional theory studies of methyl dissociation on a Ni(111) surface in the presence of an external electric field, Phys. Chem. Chem. Phys, **2016**,16, 2399-2410.